Output Ripple Analysis of Switching DC–DC Converters

Zoran Mihajlovic, *Member, IEEE*, Brad Lehman, *Member, IEEE*, and Chunxiao Sun, *Member, IEEE*

***Abstract*—State space averaging methods are used to derive time-invariant models that bound the envelope of trajectories of pulsewidth modulated (PWM) dc–dc converters. The results are compared to conventional averaging methods used in power electronics, and it is shown that, at times, designing a dc–dc converter based on the averaged output of a converter can be ineffective because peak output values sometimes significantly deviate from the averaged output. This paper attempts to quantify this deviation by using both small-signal transfer functions and nonlinear models to model the maximum and minimum values of outputs of PWM converters. Issues in simulation and control loop design are also mentioned.**

***Index Terms*—Approximation methods, DC–DC power conversion, modeling, pulsewidth modulation.**

I. Introduction

THE procedure of averaging switch-mode power supplies introduces a design paradigm: control loops are simple to design because they can utilize Bode and other frequency-domain plots, based on the linearization of an averaged differential equation. This leads to performance guarantees for the *averaged* system. However, the performance must be evaluated on the actual switching (time-varying) circuit and not the averaged dynamics. Hence, it is possible to design a control loop that guarantees performance criteria for the averaged dynamics, but the power circuit may still have unsuitable peak-to-peak deviations. A typical example of this might be when the load resistance suddenly decreases. Although an integral controller may guarantee that the averaged output voltage remains constant, the effects of the equivalent series resistance (ESR) of the capacitor will cause deviations in the minimum and maximum values of the output voltage. In some applications, these deviations are unsuitable, especially in instances where dc–dc converters are used to precisely regulate output voltage, e.g., voltage regulator modules for Pentium processors have output voltage regulation requirements to within 1%.

Past research in the analysis of ripples for dc–dc converters [7], [8], [18], [17], [3] primarily focuses on ideal converters and their state ripples. Our emphasis in this paper is to study the ripples in the output equation in the nonideal case when parasitics are included in the modeling. We show that these ripples can have behavior contrary to the averaged response. As a result, *it is incorrect to assume that a dc–dc converter design that is based on the averaged output response will necessarily maintain peak ripple values within satisfactory bounds.* In fact, a typical dc–dc converter design procedure is first to design a control loop based on the averaged converter dynamics and then perform extensive trial and error numerical simulations under worst case scenarios (e.g., shorts, and current disturbances) to verify that the output signals of the switching circuit behave correctly. This becomes time-consuming since it is necessary to simulate the switching system, and not the averaged system, to verify that maximum and minimum values of currents and voltages are within desired bounds.

The philosophy of this present research is simple: in order to understand and control the maximum and minimum values of output signals, it is vital to model peak signal values. The scope of this paper is to present new *averaged* models which are able to reflect these peak characteristics and, furthermore, that these models be *time-invariant*. The approach of this paper is to utilize the Krylov–Bogoliubov–Mitropolsky (KBM) [1] method of averaging to provide asymptotic approximations of ripple models. Then envelopes are created of these ripples that bound the maximum and minimum ripple value. These envelopes are superimposed on the conventional averaged models to create new models that predict the maximum, averaged, and minimum behavior of pulsewidth modulated (PWM) converters. Rigorous mathematical justification is presented for the models, and experiments verify their accuracy.

The idea of creating "envelopes" for power converters has also been proposed by [15] and [6] and, hence, has proven merit. In [15], the technique of generalized averaging is used to write differential equations for (complex) Fourier series coefficients, and envelopes are obtained by increasing the order of the differential equation. In [6], a first-order approximation of a matrix exponential is used to derive an envelope. This technique is shown to have computational advantages for simulations. Our approach complements both these methods, providing dynamic accuracy and simulation efficiency. Specifically, we rely on formal KBM averaging methods instead of generalized averaging and exponential approximations. As a result, we derive new envelope models that have the same state differential equation as conventional averaged models [13], [5], but have a different output equation. This is in contrast to the method of [15] which increases the order of the state differential equation to derive the envelope. In some sense, our results maintain some simplicity of traditional averaging methods, while at the same time receive the computational time benefits of the envelope method documented by [6]. Additionally, it is our belief that there is added benefit to presenting a modeling method that is substantiated by rigorous theoretical proofs. As noted in [5], this is sometimes missing in the power electronics community.

Manuscript received February 3, 2001; revised November 22, 2003. This paper was recommended by Associate Editor D. Czarkowski.

Z. Mihajlovic is with Texas Instruments Incorporated, Warrenville, IL 60089 USA.

B. Lehman is with the Department of Electrical and Computer Engineering, Northeastern University, Boston, MA 02115 USA (e-mail: lehman@ece.neu.edu).

C. Sun is with Danaher Corporation, Wilmington, MA 01887 USA.

Digital Object Identifier 10.1109/TCSI.2004.832792

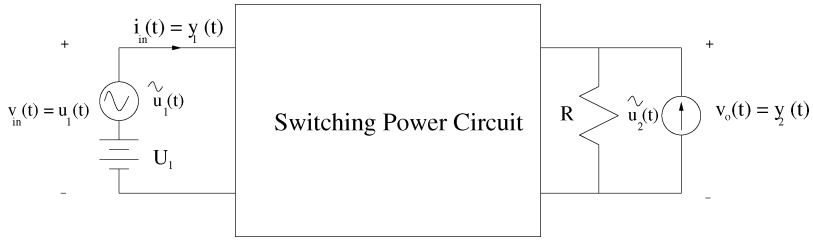

Fig. 1. General diagram of the multi-input, multi-output dc–dc switching converter.

Section II presents step-by-step procedures for modeling the envelopes and ripples of dc–dc converters in continuous conduction mode (CCM). (We do not consider multilevel/multiswitch converters. Further, we only consider hard switched converters in CCM, although the the algorithm presented may be extended to converters operating in discontinuous conduction mode or utilizing soft switching.) Section III presents experimental verification of the large-signal models and of newly proposed small-signal transfer functions for the envelope models. These new small-signal transfer functions characterize the behavior of minimum and maximum output signal values subject to small-signal disturbances. This permits a designer to better understand the effects of parasitics, short circuits, and other disturbances on peak output signals. To our knowledge, this is the first time that transfer functions such as these have appeared in the literature. Their benefits, though, are apparent. Section IV presents further discussion on closed-loop design and simulation issues. Section V presents conclusions.

II. Modeling Output Ripples

In this section, we present a step-by-step algorithm to model outputs of PWM systems that switch between two linear differential equations. Our motivation is switching dc–dc converters, but the broader applications are apparent since nothing restricts us to dc–dc converters. For example, dc motor drives with pulsewidth modulation also have similar models [14].

The goal of this section is to create formal averaging procedures, with rigorous mathematical justification, that do not lose ripple information for outputs. In Section II-A, the modeling algorithm is presented for large-signal modeling, and theoretical proofs are given. The new contribution of the models is to create time-invariant envelope models that bound the peak values of the PWM output. Section II-B utilizes these new models to derive small-signal equations and demonstrates how the new models provide insight to analysis and design of dc–dc converters that were not possible with previously known models.

The algorithm is broken into two categories: large-signal modeling and small-signal modeling. Steps 1 and 2 are previously known and can be found in [13] and [5].

A. Large Signal Modeling

1) Algorithm:

Step 1: Derive a State Space Description for Each Circuit State: Assume that the dc–dc converter is in CCM and has two circuit states: switch on or switch off. (Even if soft switching is utilized, the zero-voltage or zero-current state is often such a short instance of time that it might not be modeled.) Therefore, the state space description can be written as

$$\left.\begin{aligned}\dot{\mathbf{x}} &= \mathbf{A}_1\mathbf{x}+\mathbf{B}_1\mathbf{u}+\mathbf{G}_1,\\ \mathbf{y} &= \mathbf{C}_1\mathbf{x}+\mathbf{F}_1\mathbf{u},\end{aligned}\right\}, \qquad 0 \le t \bmod(T) < d\cdot T$$

$$\left.\begin{aligned}\dot{\mathbf{x}} &= \mathbf{A}_2\mathbf{x}+\mathbf{B}_2\mathbf{u}+\mathbf{G}_2,\\ \mathbf{y} &= \mathbf{C}_2\mathbf{x}+\mathbf{F}_2\mathbf{u},\end{aligned}\right\}, \qquad d\cdot T \le t \bmod(T) < T$$

where $\mathbf{x} \in \Re^n$, $d \in \Re$, is the duty ratio function satisfying $0 \le d \le 1$, and T is the period. Since d can be a function of $\mathbf{x}$, the above model is valid in either open or closed loop. Parasitic elements such as equivalent series resistance of the filter capacitor, and diode forward voltage should also be included. For example, using the voltage plus resistance model for the diode introduces the matrices $\mathbf{G}_1$ and $\mathbf{G}_2$. For dc–dc converters, the output vector, $\mathbf{y} \in \Re^m$, is often assumed to be $\mathbf{y} = [y_1\ y_2]^T = [i_{\text{in}}\ v_o]^T$, where i_{in} is the input current and v_o is the output voltage. The input vector, $\mathbf{u} \in \Re^p$, is often assumed to be $\mathbf{u} = [u_1\ u_2]^T = [v_{\text{in}}\ i_o]^T$. Fig. 1 illustrates the typical input/output characteristics of a dc–dc converter. Normally, it is assumed that u_1 has dc and ac components. That is, $u_1(t) = U_1 + \tilde{u}_1(t)$, where U_1 is constant. On the other hand, u_2 is often considered to be an ac perturbation only, i.e., $u_2(t) = \tilde{u}_2(t)$. As a matter of notation, all matrices and vectors are written in bold, while scalar valued variables and functions are written in normal font.

Step 2: Average: For a sufficiently small switching period, $\mathbf{x}(t) \approx \bar{\mathbf{x}}(t)$, where $\bar{\mathbf{x}}(t)$ is given as the solution to the "averaged equation" as follows:

$$\dot{\bar{\mathbf{x}}} = \mathbf{A}(d)\bar{\mathbf{x}} + \mathbf{B}(d)\mathbf{u} + \mathbf{G}(d) \tag{1}$$

and $\mathbf{A}(d) \equiv \mathbf{A}_1 d + \mathbf{A}_2(1-d)$, $\mathbf{B}(d) \equiv \mathbf{B}_1 d + \mathbf{B}_2(1-d)$, $\mathbf{G}(d) \equiv \mathbf{G}_1 d + \mathbf{G}_2(1-d)$, and $d = d(\bar{\mathbf{x}})$. This, of course, is the classical averaged model given by [11]. Similarly, [13] and [12] give the averaged output equation as

$$\bar{\mathbf{y}} = \mathbf{C}(d)\bar{\mathbf{x}} + \mathbf{F}(d)\mathbf{u} \tag{2}$$

where $\mathbf{C}(d) \equiv \mathbf{C}_1 d + \mathbf{C}_2(1-d)$ and $\mathbf{F}(d) \equiv \mathbf{F}_1 d + \mathbf{F}_2(1-d)$.

Step 3: Compute a State Ripple Estimate: Extending the results of [7] to the case when $\mathbf{u}$ is a function of time (see theorem in next subsection), it is proposed to estimate the difference

$$\begin{aligned}\mathbf{x}(t) - \bar{\mathbf{x}}(t) &= \mathbf{\Psi}_x(\bar{\mathbf{x}}, d, \mathbf{u}, t)\\ &\approx T[(\mathbf{A}_1-\mathbf{A}_2)\bar{\mathbf{x}} + (\mathbf{B}_1-\mathbf{B}_2)\mathbf{u} + (\mathbf{G}_1-\mathbf{G}_2)]\\ &\quad\cdot\Big\{[h(d-\text{tri}(t,T))-d]\text{tri}(t,T)\\ &\quad + [1-h(d-\text{tri}(t,T))]d + \frac{1}{2}d(d-1)\Big\}\end{aligned} \tag{3}$$

where $d = d(\bar{\mathbf{x}})$ and h is the Heaviside step function, that is, $h(s) = 1$ for $s > 0$ and $h(s) = 0$ for $s < 0$. The function $\text{tri}(t,T) = t/T - \text{floor}(t/T) = (t \text{mod} T)/T$. $\boldsymbol{\Psi}_x$ is called the "state ripple."

Theoretical justification of the state ripple estimate is based on KBM averaging algorithms [1] applied to PWM switching converters in [8]: when there is no chattering, the model in **Step 1** is a state discontinuous differential equation given by

$$\dot{\mathbf{x}} = (\mathbf{A}_2\mathbf{x} + \mathbf{B}_2\mathbf{u} + \mathbf{G}_2) + [(\mathbf{A}_1 - \mathbf{A}_2)\mathbf{x} + (\mathbf{B}_1 - \mathbf{B}_2)\mathbf{u}(\mathbf{G}_1 - \mathbf{G}_2)]h(d(\mathbf{x}) - \text{tri}(t,T)) \quad (4)$$

with output equation

$$\mathbf{y} = \mathbf{C}_2\mathbf{x} + \mathbf{F}_2\mathbf{u} + [(\mathbf{C}_1 - \mathbf{C}_2)\mathbf{x} + (\mathbf{F}_1 - \mathbf{F}_2)\mathbf{u}] \cdot h(d(\mathbf{x}) - \text{tri}(t,T)). \quad (5)$$

Since the state ripple is defined as $\boldsymbol{\Psi}_x(\bar{\mathbf{x}}, d, \mathbf{u}, t) = \mathbf{x}(t) - \bar{\mathbf{x}}(t)$, it is possible to determine $\boldsymbol{\Psi}_x$ using the formula: $\boldsymbol{\Psi}_x = \int^t (\dot{\mathbf{x}}(s) - \dot{\bar{\mathbf{x}}}(s))ds + \mathbf{K}(\bar{\mathbf{x}}, d, \mathbf{u})$, where $\mathbf{K}(\bar{\mathbf{x}}, d, \mathbf{u})$ is a function chosen to make $\boldsymbol{\Psi}_x$ zero average. We now assume that, over any period, $\mathbf{x}(t) = \bar{\mathbf{x}}$ is constant and likewise that $\mathbf{u}$ and d are constant also. Then, taking the integral of the difference between the right-hand sides of (4) and (1) will exactly lead to the estimate of the state ripple given above. (This requires a significant amount of algebra that has been omitted.)

Step 4: Compute the Output Ripple: Once an estimate of the state ripple has been derived, this research proposes that an improved estimate of the output can be given by $\mathbf{y} = \bar{\mathbf{y}} + \bar{\boldsymbol{\Psi}}_y$, where $\bar{\boldsymbol{\Psi}}_y$ is obtained by taking the difference of (5) and (2) as follows:

$$\begin{aligned}\mathbf{y}(t) - \bar{\mathbf{y}}(t) &= \boldsymbol{\Psi}_{bfy}(\bar{\mathbf{x}}, d, \mathbf{u}, t) \\ &= \mathbf{C}_2\mathbf{x} + [(\mathbf{C}_1 - \mathbf{C}_2)\mathbf{x} + (\mathbf{F}_1 - \mathbf{F}_2)\mathbf{u}] \\ &\quad \cdot h(d(\mathbf{x}) - \text{tri}(t,T)) + \mathbf{F}_2\mathbf{u} \\ &\quad - [\mathbf{C}_1 d(\bar{\mathbf{x}}) + \mathbf{C}_2(1 - d(\bar{\mathbf{x}}))]\bar{\mathbf{x}} \\ &\quad - [\mathbf{F}_1 d(\bar{\mathbf{x}}) + \mathbf{F}_2(1 - d(\bar{\mathbf{x}}))]\mathbf{u}. \end{aligned} \quad (6)$$

Using the estimate $\mathbf{x} = \bar{\mathbf{x}} + \boldsymbol{\Psi}_x$ and $d(\mathbf{x}) + d(\bar{\mathbf{x}})$ yields

$$\begin{aligned}\boldsymbol{\Psi}_y(\bar{\mathbf{x}}(t), d, \mathbf{u}, t) &= \mathbf{C}_2\boldsymbol{\Psi}_x + [(\mathbf{C}_1 - \mathbf{C}_2)(\bar{\mathbf{x}} + \boldsymbol{\Psi}_x) \\ &\quad + (\mathbf{F}_1 - \mathbf{F}_2)\mathbf{u}]h(d(\bar{\mathbf{x}}) - \text{tri}(t,T)) \\ &\quad - (\mathbf{C}_1 - \mathbf{C}_2)\bar{\mathbf{x}}d(\bar{\mathbf{x}}) - (\mathbf{F}_1 - \mathbf{F}_2)\mathbf{u}d(\bar{\mathbf{x}}) \end{aligned} \quad (7)$$

where $\boldsymbol{\Psi}_x$ is given in **Step 3**. This leads to the estimate $\mathbf{y} \approx \bar{\mathbf{y}} + \boldsymbol{\Psi}_y$, with $\boldsymbol{\Psi}_y$ as above. The interesting aspect of this new modeling method is that it gives insight to the instantaneous values and peak values of the output $\mathbf{y}$ which are not attainable using classical averaged models.

Step 5: Model the Envelope Functions $\mathbf{y}_{\max}(t)$ *and* $\mathbf{y}_{\min}(t)$*:* The ripple $\boldsymbol{\Psi}_y$ depends on both fast variables (t) and slow variables ($\bar{\mathbf{x}}, d, \mathbf{u}$). For sufficiently small switching period T, these slow harmonics can be viewed as constant on a cycle-by-cycle basis. Hence, on a cycle-by-cycle basis, $\boldsymbol{\Psi}_y$ can be viewed as purely a function of time. Since $\bar{\mathbf{y}}$ can be viewed as constant on a cycle-by-cycle basis, this implies that each component of $\mathbf{y}$, given by $y_i \approx \bar{y}_i + \Psi_{yi}$, obtains its max/min whenever Ψ_{yi} obtains its max/min, for $i = 1, 2, \ldots, m$.

To formalize this concept, let $\mathbf{c}_1 \in \Re^n$, $c_2 \in \Re$, and $\mathbf{c}_3 \in \Re^m$ be constant vectors, and assume $0 < c_2 < 1$. Define

$$\begin{aligned}\Psi_{yi_{\max}}(\mathbf{c}_1, c_2, \mathbf{c}_3) &\equiv \sup_{t\in[0,T]} \Psi_{yi}(\mathbf{c}_1, c_2, \mathbf{c}_3, t) \\ \Psi_{yi_{\min}}(\mathbf{c}_1, c_2, \mathbf{c}_3) &\equiv \inf_{t\in[0,T]} \Psi_{yi}(\mathbf{c}_1, c_2, \mathbf{c}_3, t). \end{aligned} \quad (8)$$

Hence, we can create new functions

$$\begin{aligned}y_{i\,\max}(t) &= \bar{y}_i(t) + \Psi_{yi_{\max}}(\bar{\mathbf{x}}(t), d(\bar{\mathbf{x}}(t)), \mathbf{u}(t)), \\ y_{i\,\min}(t) &= \bar{y}_i(t) + \Psi_{yi_{\min}}(\bar{\mathbf{x}}(t), d(\bar{\mathbf{x}}(t)), \mathbf{u}(t)) \end{aligned} \quad (9)$$

or, in vector notation

$$\begin{aligned}\mathbf{y}_{\max}(t) &= \mathbf{C}(d)\bar{\mathbf{x}} + \mathbf{F}(d)\mathbf{u} + \boldsymbol{\Psi}_{y_{\max}} \\ \mathbf{y}_{\min}(t) &= \mathbf{C}(d)\bar{\mathbf{x}} + \mathbf{F}(d)\mathbf{u} + \boldsymbol{\Psi}_{y_{\min}} \end{aligned} \quad (10)$$

where $\boldsymbol{\Psi}_{y_{\max}} = [\Psi_{y1_{\max}}\ \Psi_{y2_{\max}} \ldots \Psi_{ym_{\max}}]^T$ and $\boldsymbol{\Psi}_{y_{\min}} = [\Psi_{y1_{\min}} \ldots \Psi_{ym_{\min}}]^T$. Here, $\boldsymbol{\Psi}_{y_{\max/min}}$ depends explicitly on the slow variables and, therefore, can be viewed as a slowly moving envelope around $\boldsymbol{\Psi}_y$ over time. The elegance of the technique is that the envelope signals depend only on $\bar{\mathbf{x}}$, d, and $\mathbf{u}$. The state differential equations for $\bar{\mathbf{x}}$ remain the same as in (1). Only adjustments in the output equation are needed to model peak envelopes. Hence, (1) together with (2) and (10) characterize the new model.

Remark 1: It is important to recognize that the new models (1),(2), and (10) are completely *time-invariant* yet provide information on the minimum, averaged, and maximum values of a PWM converter. Also, the ripple on the output does not always tend to zero as $T \to 0$. This makes the above model/algorithm quite different than other known state space averaging results in the literature, e.g., the work of Bass *et al.* [5], [7], [8]. In these previous works, the output equation is not examined—only the state differential equation and its corresponding averaged equation are modeled. State ripples tend to zero as the switching period tends to zero.

For example, dc–dc converters with discontinuous output current, i.e., the output current must pass through a switching diode (e.g., Boost, Flyback, or Cuk), the ESR must cause a ripple to occur, even as the switching period tends to zero. In the steady state, this is simple to understand: the output capacitor with ESR is placed in parallel with the resistive load (R). Since, in steady state, the capacitor has zero average current through it, this implies that the average current through the ESR is zero. Hence, the ESR has zero average voltage across it, and the average output voltage is equal to the average capacitor voltage $V_C = V_o$. On the other hand, when the diode to the output filter is open, on the interval $DT \leq t \text{mod} T \leq T$, there is no supply current and simple voltage division will lead to $V_{o_{\min}} = V_C(R/(R + ESR))$, which represents the minimum steady-state value of the output voltage when there is no ripple on the capacitor voltage. Therefore, in order to maintain the average output voltage to be $V_o = V_C$ in steady state, it is necessary, on the interval $0 \leq tmodT \leq DT$, that $V_C = V_{o_{\max}}(1 + (\text{ESR}(1 - D))/(D(R + \text{ESR})))$, which is the maximum steady-state value of the output voltage when there are no inductor or capacitor ripples. Hence, an output ripple must always occur.

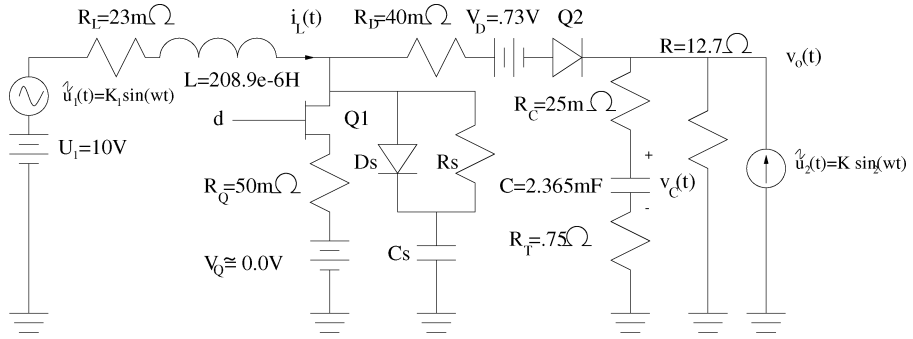

Fig. 2. Benchmark boost converter.

Finally, notice that Ψ_{yi} attains its maximum and minimum values either at $t = 0^+ \mathrm{mod} T$ or $t = dT^- \mathrm{mod} T$ or $t = dT^+ \mathrm{mod} T$ or $t = T^- \mathrm{mod} T$. This is derived from the fact that Ψ_{xi} is a zero average triangle wave and the fact that $\boldsymbol{\Psi}_x$ and $\bar{\boldsymbol{\Psi}}_y$ switch at the same instant of time. For example, in the boost converter in Fig. 2, the maximum and minimum output voltage is given as $y_{2\max} = v_{o_{\max}} \approx \mathbf{C}(d)\mathbf{x} + \boldsymbol{\Psi}_y(\mathbf{x}, d, \mathbf{u}, t_{2\max} = dT^+)$, and $y_{2\min} = v_{o_{\min}} \approx \mathbf{C}(d)\mathbf{x} + \boldsymbol{\Psi}_y(\mathbf{x}, d, \mathbf{u}, t_{2\min} = dT^-)$, respectively. Likewise, the input current has a minimum at $t_{1\min} = TmodT$ and a maximum value at $t_{1\max} = dT$. (The input current is continuous.) In a buck converter $t_{1\max} = t_{2\max} = dT \mathrm{mod} T$ and $t_{2\min} = T \mathrm{mod} T$.

2) Theoretical Foundations: In this subsection, formal mathematical theorems are presented to justify the above modeling algorithm. A difficulty in applying formal state space averaging methods is that the switching time in a dc–dc converter occurs when $d = \mathrm{tri}(t, T)$, as in (4). In a closed loop, $d = d(\mathbf{x})$ and hence (4) represents a state-discontinuous differential equation. As in [7], we will need to utilize the methods of Filippov [4] to average dc–dc converters. Specifically, for sufficiently small switching period, T, the right-hand side of (4) is continuous almost everywhere. Hence, a continuous solution $\mathbf{x}(t)$ exists, which satisfies (4) almost everywhere.

For simplicity, define operators $\mathcal{J} : \Re^n \times \Re^p \to \Re^n$ and $\mathcal{W} : \Re^n \times \Re^p \to \Re^n$ as

$$\begin{aligned}\mathcal{J}(\mathbf{x}, \mathbf{u}) \equiv \int_0^t & (\mathbf{A}_2\mathbf{x}(s) + \mathbf{B}_2\mathbf{u}(s) + \mathbf{G}_2 \\ & + [(\mathbf{A}_1 - \mathbf{A}_2)\mathbf{x}(s) + (\mathbf{B}_1 - \mathbf{B}_2)\mathbf{u}(s) + (\mathbf{G}_1 - \mathbf{G}_2)] \\ & \cdot h(d(\mathbf{x}(s)) - \mathrm{tri}(s, T)))ds \end{aligned} \tag{11}$$

$$\begin{aligned}\mathcal{W}(\bar{\mathbf{x}}, \mathbf{u}) \equiv \int_0^t & [\mathbf{A}(d(\bar{\mathbf{x}}(s)))\bar{\mathbf{x}}(s) + \mathbf{B}(d(\bar{\mathbf{x}}(s)))\mathbf{u}(s) \\ & + \mathbf{G}(d(\bar{\mathbf{x}}(s)))]ds \end{aligned} \tag{12}$$

where $\mathbf{A}(d)$, $\mathbf{B}(d)$, and $\mathbf{G}(d)$ are as given in **Step 2**. Occasionally we will write $\mathcal{J}_{[t_1,t_2]}(\cdot)$ or $\mathcal{W}_{[t_1,t_2]}(\cdot)$ to indicate that the above integrations take place between $t = t_1$ and $t = t_2$. If no time interval is given, then it can be assumed that $t_1 = 0$ and $t_2 = t$. In this notation, $\mathcal{J}(\cdot) \equiv \mathcal{J}_{[0,t]}(\cdot)$.

For a sufficiently small switching period T, the solutions $\mathbf{x}(t) = \mathbf{x}(0) + \mathcal{J}(\mathbf{x}, \mathbf{u})$ and $\bar{\mathbf{x}}(t) = \bar{\mathbf{x}}(0) + \mathcal{W}(\bar{\mathbf{x}}, \mathbf{u})$ are continuous and satisfy differential equations (4) and (1) almost everywhere, respectively. (The reader is referred to [7] for a detailed proof/discussion of this statement.)

Theorem 1: Let $\mathbf{x}(t)$, $\mathbf{y}(t)$, $\bar{\mathbf{x}}(t)$, and $\bar{\mathbf{y}}(t)$ be the (almost everywhere) solutions of (4), (5), (1), and (2), respectively, with $\mathbf{x}(0) = \bar{\mathbf{x}}(0)$, and assume that $\mathbf{x}(t)$ is continuous almost everywhere. Let $\boldsymbol{\Psi}_x$ and $\boldsymbol{\Psi}_y$ be as defined in (3) and (7), respectively. Suppose that duty ratio $d(\mathbf{x})$ is continuous, Lipschitz, and satisfies $0 < d < 1$ for all $\mathbf{x}$ in compact sets of $\Re^n$. Suppose further that $\mathbf{u}(t) \in \Re^n$ is continuous, bounded, and independent of switching period T. Then, for any $L > 0$ and $\eta > 0$, there exists a $T_0 = T_0(\eta, L)$ such that, for a sufficiently small switching period satisfying $0 < T \le T_0$, we can make the following conclusions:

1) $|\mathbf{y}(t) - \bar{\mathbf{y}}(t) - \boldsymbol{\Psi}_y(\bar{\mathbf{x}}(t), d(\bar{\mathbf{x}}(t)), \mathbf{u}, t)| \le \eta$ for any $0 \le t \le L$;
2) $|\sup_{0\le\sigma<T} y_i(t+\sigma) - y_{i\max}(t)| \le \eta$ and $|\inf_{0\le\sigma<T} y_i(t+\sigma) - y_{i\min}(t)| \le \eta$ for any $0 \le t \le L$, $i = 1, 2, \ldots m$, where $y_{i\max}$ and $y_{i\min}$ are defined in **Step 5** and y_i is a component of $\mathbf{y}$;
3) if, in addition, $\bar{\mathbf{x}}(t)$ approaches a uniformly asymptotically stable equilibrium point, then the above conclusions 1), and 2) remain valid for all $t \ge 0$.

Proof: Proof of Conclusion 1) : The work of [7] shows that for any $\delta > 0$ there exists a $T_0 = T_0(\delta)$ such that, for $0 < T < T_0$, $|\mathcal{J}(\mathbf{x}, \mathbf{c}) - \mathcal{W}(\bar{\mathbf{x}}, \mathbf{c})| \le \delta$ for any $t_0 \le t \le t_0 + L$, where $\mathbf{c} \in \Re^p$ is a constant vector. First, we will extend this result to permit $\mathbf{c} = \mathbf{u}$ to be time-varying. Then we will prove Conclusion 1).

Since $\mathbf{u}$ is a continuous function of time, we can always find a piecewise constant function $\hat{\mathbf{u}}(t) \in \Re^m$ such that, for any $\mu > 0$, $|\mathbf{u}(t) - \hat{\mathbf{u}}(t)| \le \mu$ for all $0 \le t \le L$ [2]. Furthermore, there will exist a sequence of time $0 = a_0 < a_1 < a_2 \cdots < a_r = t \le L$ and a set of constant vectors $\mathbf{c}_j \in \Re^n$, $j = 1, 2, \ldots, r$, with $\mathbf{c}_j = \hat{\mathbf{u}}(t)$ on the interval $t \in [a_{j-1}, a_j)$. This implies that

$$\begin{aligned}|\mathbf{x}(t) - \bar{\mathbf{x}}(t)| &= |\mathbf{x}(0) - \bar{\mathbf{x}}(0) + \mathcal{J}(\mathbf{x}, \mathbf{u}) - \mathcal{W}(\bar{\mathbf{x}}, \mathbf{u})| \\ &\le |\mathcal{J}(\mathbf{x}, \mathbf{u}) - \mathcal{J}(\mathbf{x}, \hat{\mathbf{u}})| + |\mathcal{J}(\mathbf{x}, \hat{\mathbf{u}}) - \mathcal{W}(\bar{\mathbf{x}}, \hat{\mathbf{u}})| \\ &\quad + |\mathcal{W}(\bar{\mathbf{x}}, \hat{\mathbf{u}}) - \mathcal{W}(\bar{\mathbf{x}}, \mathbf{u})|. \end{aligned} \tag{13}$$

But, by construction of $\hat{\mathbf{u}}$, we have

$$\begin{aligned}|\mathcal{J}(\mathbf{x}, \mathbf{u}) - \mathcal{J}(\mathbf{x}, \hat{\mathbf{u}})| &\le \int_0^t [B_2 + (B_1 - B_2)h(\cdot)] \cdot (\mathbf{u}(s) - \hat{\mathbf{u}}(s))ds \\ &\le L(|B_1| + |B_1 - B_2|)\mu = LM_1\mu \end{aligned}$$

for any $t \in [0, L]$. Likewise, $|\mathcal{W}(\bar{\mathbf{x}}, \hat{\mathbf{u}}) - \mathcal{W}(\bar{\mathbf{x}}, \mathbf{u})| \leq LM_2\mu$ for all $t \in [0, L]$. Now we remark that

$$|\mathcal{J}_{[0,t]}(\mathbf{x}, \hat{\mathbf{u}}) - \mathcal{W}_{[0,t]}(\bar{\mathbf{x}}, \hat{\mathbf{u}})| = \left| \sum_{j=1}^{r} \mathcal{J}_{[a_{j-1},a_j)}(\mathbf{x}, \mathbf{c}_j) - \mathcal{W}_{[a_{j-1},a_j)}(\bar{\mathbf{x}}, \mathbf{c}_j) \right|.$$

Since $\mathcal{J}_{[a_{j-1},a_j)}(\mathbf{x}, \mathbf{c}_j)$ and $\mathcal{W}_{[a_{j-1},a_j)}(\bar{\mathbf{x}}, \mathbf{c}_j)$ depend on constant vectors $\mathbf{c}_j$ and not $\mathbf{u}(t)$, the results of [7] can be applied, i.e., $|\mathcal{J}_{[a_{j-1},a_j)}(\mathbf{x}, \mathbf{c}_j) - \mathcal{W}_{[a_{j-1},a_j)}(\bar{\mathbf{x}}, \mathbf{c}_j)| \leq \delta_j(T)$. Therefore, $|\mathcal{J}_{[0,t]}(\mathbf{x}, \hat{\mathbf{u}}) - \mathcal{W}_{[0,t]}(\bar{\mathbf{x}}, \hat{\mathbf{u}})| \leq \delta(T) = \sum_{j=1}^{r} \delta_j$ for any $0 \leq t \leq L$. Furthermore, $\delta(T) \to 0$ as $T \to 0$. Hence, (13) leads to $|\mathbf{x}(t) - \bar{\mathbf{x}}(t)| \leq \mu L(M_1 + M_2) + \delta(T) = \sigma(\mu, T)$. This bound can be made arbitrarily small by constructing $\hat{\mathbf{u}}$ so that μ is arbitrarily small and by selecting T sufficiently small. [1]

Now we complete the proof of Conclusion 1): using (6) and (7), we have

$$\begin{aligned} &|\mathbf{y}(t) - \bar{\mathbf{y}}(t) - \mathbf{\Psi}_y(\cdot)| \\ &\quad = |\mathbf{C}_2[\mathbf{x}(t) - \bar{\mathbf{x}}(t) - \mathbf{\Psi}_x(\cdot)] + (\mathbf{C}_1 - \mathbf{C}_2) \\ &\qquad \cdot h(d(\mathbf{x}(t)) - \mathrm{tri}(t, T))[\mathbf{x}(t) - \bar{\mathbf{x}}(t) - \mathbf{\Psi}_x(\cdot)]| \\ &\quad \leq (|\mathbf{C}_2| + |\mathbf{C}_1 - \mathbf{C}_2|)[|\mathbf{x}(t) - \bar{\mathbf{x}}(t)| + |\mathbf{\Psi}_x(\cdot)|). \end{aligned}$$

$\mathbf{\Psi}_x$ in (3) is a continuous periodic function linearly multiplied by parameter T. Therefore, for all $|\bar{\mathbf{x}}| \leq B$, $B > 0$, we have $|\mathbf{\Psi}_x(\cdot)| \leq TM_3$. (It is a straightforward exercise to show that, for $0 \leq t \leq L$, there exist positive constants K_1 and K_2 such that $|\bar{\mathbf{x}}(t)| \leq B = (|x(t_0)| + K_1 \exp\{K_2 L\})$, e.g., see the lemma in [7, Appendix].) Hence, (13) leads to

$$\begin{aligned} &|\mathbf{y}(t) - \bar{\mathbf{y}}(t) - \mathbf{\Psi}_y(\cdot)| \\ &\quad \leq (|\mathbf{C}_2| + |\mathbf{C}_1 - \mathbf{C}_2|)(\sigma(\mu, T) + TM_3) = \eta_1(T) \end{aligned} \quad (14)$$

which completes the proof since $\eta_1(T) \to 0$ as $T \to 0$.

Proof of Conclusion 2) : We prove only $|\sup_{0 \leq \sigma < T} y_i(t+\sigma) - y_{i\max}(t)| \leq \eta$, since the proof for *inf* is almost identical. Define $\tilde{y}_i(t) \equiv \bar{y}_i(t) + \Psi_{yi}(\bar{\mathbf{x}}, d(\bar{\mathbf{x}}), \mathbf{u}, t)$. Then

$$\begin{aligned} &|\sup_{0 \leq \sigma < T} y_i(t+\sigma) - y_{i\max}(t)| \\ &\qquad \leq |\sup_{0 \leq \sigma < T} \{y_i(t+\sigma) - \tilde{y}_i(t+\sigma)\}| \\ &\qquad\quad + |\sup_{0 \leq \sigma < T} \tilde{y}_i(t+\sigma) - y_{i\max}(t)|. \end{aligned} \quad (15)$$

By the proof of Conclusion 1), we have $|\sup_{0 \leq \sigma < T} \{y_i(t + \sigma) - \tilde{y}_i(t + \sigma)\}| \leq \eta_1(T)$, for any $0 \leq t \leq L$, where $\eta_1(T) \to 0$ as $T \to 0$. For simplicity, define the vector $\mathbf{g}^T(t) = [\bar{\mathbf{x}}^T(t)\ d(\bar{\mathbf{x}}(t))\ \mathbf{u}^T(t)]$. Then we have

$$\begin{aligned} &|\sup_{0 \leq \sigma < T} \tilde{y}_i(t+\sigma) - y_{i\max}(t)| \\ &\quad = |\sup_{0 \leq \sigma < T} \{\bar{y}_i(t+\sigma) + \Psi_{yi}(\mathbf{g}(t+\sigma), t+\sigma)\} \\ &\qquad - \{\bar{y}_i(t) + \sup_{0 \leq s < T} \Psi_{yi}(\mathbf{g}(t), t+s)\}| \\ &\quad \leq |\sup_{0 \leq \sigma < T} \bar{y}_i(t+\sigma) - \bar{y}_i(t)| \\ &\qquad + |\sup_{0 \leq \sigma < T} \Psi_{yi}(\mathbf{g}(t+\sigma), t+\sigma) \\ &\qquad - \sup_{0 \leq s < T} \Psi_{yi}(\mathbf{g}(t), t+s)|. \end{aligned} \quad (16)$$

The solution $\bar{y}_i(t)$ is a continuous function of time t and is independent of switching period T. This is also true for $\bar{\mathbf{x}}(t)$, which for any finite time interval will remain in a closed bounded set $|\bar{\mathbf{x}}| \leq B$. Therefore, by continuity, $|\sup_{0 \leq \sigma < T} \bar{y}_i(t + \sigma) - \bar{y}_i(t)| \leq \eta_2(T)$ for any $0 \leq t \leq L$, where $\eta_2(T) \to 0$ as $T \to 0$.

Next we must analyze the second term on the right-hand side of the above inequality (16). This is not so simple since Ψ_{yi} is neither continuous nor Lipschitz. (In fact, the inequality would not be true if the *sup's* were not included.) On the other hand, using (7), it is possible to write

$$\Psi_{yi}(\mathbf{g}(t), t) = f_1(\mathbf{g}(t), t) + f_2(\mathbf{g}(t), t) h(g_{n+1}(t) - tri(t, T))$$

where $g_{n+1} = d(\bar{\mathbf{x}})$ and

$$\begin{aligned} f_1(\mathbf{g}, t) &\equiv \mathbf{e^i}[\mathbf{C}_2 \mathbf{\Psi}_x(\mathbf{g}(t), t) - (\mathbf{C}_1 - \mathbf{C}_2)\bar{\mathbf{x}} d(\bar{\mathbf{x}}) \\ &\qquad - (\mathbf{F}_1 - \mathbf{F}_2)\mathbf{u} d(\bar{\mathbf{x}})] \\ f_2(\mathbf{g}, t) &\equiv \mathbf{e^i}[(\mathbf{C}_1 - \mathbf{C}_2)(\bar{\mathbf{x}} + \mathbf{\Psi}_x(\mathbf{g}(t), t)) + (\mathbf{F}_1 - \mathbf{F}_2)\mathbf{u}] \end{aligned}$$

and $\mathbf{e^i} \in \Re^{1 \times m}$ with $\mathbf{e^i} = [e_1^i\ e_2^i \ldots e_m^i]$, where $e_k^i = 0$, when $k \neq i$ and $e_k^i = 1$, when $k = i$, for $i, k = 1, 2, \ldots m$. The functions f_1 and f_2 are continuous with respect to all their variables. Hence,

$$\begin{aligned} &|\sup_{0 \leq \sigma < T} \Psi_{yi}(\mathbf{g}(t+\sigma), t+\sigma) - \sup_{0 \leq s < T} \Psi_{yi}(\mathbf{g}(t), t+s)| \\ &\quad \leq |\sup_{0 \leq \sigma < T} f_1(\mathbf{g}(t+\sigma), t+\sigma) - \sup_{0 \leq s < T} f_1(\mathbf{g}(t), t+s)| \\ &\quad + |\sup_{0 \leq \sigma < T} f_2(\mathbf{g}(t+\sigma), t+\sigma) h(g_{n+1}(t+\sigma) \\ &\quad - tri(t+\sigma, T)) - \sup_{0 \leq s < T} f_2(\mathbf{g}(t), t+s) \\ &\quad \cdot h(g_{n+1}(t) - tri(t+s, T))|. \end{aligned} \quad (17)$$

Using the definition of f_1, we see that

$$\begin{aligned} &|\sup_{0 \leq \sigma < T} f_1(\mathbf{g}(t+\sigma), t+\sigma) - \sup_{0 \leq s < T} f_1(\mathbf{g}(t), t+s)| \\ &\quad \leq |\mathbf{C}_2| \cdot |\sup_{0 \leq \sigma < T} \mathbf{\Psi}_x(\mathbf{g}(t+\sigma), t+\sigma) \\ &\quad - \sup_{0 \leq s < T} \mathbf{\Psi}_x(\mathbf{g}(t), t+s)| + |\mathbf{C}_1 - \mathbf{C}_2| \\ &\quad \cdot |\sup_{0 \leq \sigma < T} \bar{\mathbf{x}}(t+\sigma) d(\bar{\mathbf{x}}(t+\sigma)) - \bar{\mathbf{x}}(t) d(\bar{\mathbf{x}}(t))| \\ &\quad + |\mathbf{F}_1 - \mathbf{F}_2| \cdot |\sup_{0 \leq s < T} \mathbf{u}(t+s) d(\bar{\mathbf{x}}(t+s)) - \mathbf{u}(t) d(\bar{\mathbf{x}}(t))|. \end{aligned}$$

Since $\mathbf{\Psi}_x$, given in (3), is a continuous periodic function multiplied by T, and since $\mathbf{g}$ remains in closed and bounded sets, there exists an $M > 0$ such that $|\sup_{0 \leq \sigma < T} \mathbf{\Psi}_x(\mathbf{g}(t+\sigma), t+\sigma) - \sup_{0 \leq s < T} \mathbf{\Psi}_x(\mathbf{g}(t), t+s)| \leq MT$. Now continuity implies that

$$\begin{aligned} &|\sup_{0 \leq \sigma < T} f_1(\mathbf{g}(t+\sigma), t+\sigma) - \sup_{0 \leq s < T} f_1(\mathbf{g}(t), t+s)| \\ &\qquad \leq MT + \tilde{\eta}_3(T) \equiv \eta_3(T). \end{aligned}$$

To bound (17), we note that it has been assumed that d varies between zero and one and is Lipschitz. This guarantees that $h(d(\cdot) - tri(t = rT^+, T)) = 1$ and $h(d(\cdot) - tri(t = rT + T^-, T)) = 0$, for $r = 0, 1, 2, \ldots$ Hence, $h(\cdot)$ will switch at

least once per cycle. Furthermore, the conditions of the theorem guarantee that, for T sufficiently small, there will be only one switching per cycle [7]. Therefore

$$\begin{aligned}
&|\sup_{0\le\sigma<T} f_2(\mathbf{g}(t+\sigma),t+\sigma)h(g_{n+1}(t+\sigma)-tri(t+\sigma,T))\\
&\quad-\sup_{0\le s<T} f_2(\mathbf{g}(t),t+s)h(g_{n+1}(t)-tri(t+s,T))|\\
&\le|\sup_{0\le\sigma<T} f_2(\mathbf{g}(t+\sigma),t+\sigma)\\
&\quad-\inf_{0\le s<T} f_2(\mathbf{g}(t),t+s)|\\
&\le|\sup_{0\le\sigma<T} f_2(\mathbf{g}(t+\sigma),t+\sigma)-f_2(\mathbf{g}(t),t)|\\
&\quad+|f_2(\mathbf{g}(t),t)-\inf_{0\le s<T} f_2(\mathbf{g}(t),t+s)|\\
&\le\eta_4(T)
\end{aligned}$$

where $\eta_4(T)$ is derived similarly to $\eta_3(T)$. Letting $\eta(T)=\eta_1(T)+\eta_2(T)+\eta_3(T)+\eta_4(T)$ and using (15) and (16), proves Conclusion 2) of the theorem.

Proof of Conclusion 3): Straightforward averaging theory guarantees that, when $\bar{\mathbf{x}}(t)$ approaches a uniform asymptotic stability point, then $|\bar{\mathbf{x}}(t)-\mathbf{x}(t)|<\delta(T)$ for any $t\ge t_0$, where $\delta(T)\to 0$ as $T\to 0$. (There are numerous methods to prove this, such as induction [16] or contradiction [9]. In either case, the properties of uniform asymptotic stability are used to show that once solutions to both the averaged and time-varying equation approach a ball around an equilibrium point, then they can never leave this ball.) Since the averaging approximation becomes valid for all time, it is immediate from (14) that Conclusion 1) is true for all $t\ge 0$. This also implies the validity of Conclusion 2) for $t\ge 0$ since the proof of Conclusion 2) relies completely on continuity principles and the proof of Conclusion 1).

Remark 2: Conclusion 1) presents a computationally efficient method to estimate outputs of PWM dc–dc converters. For sufficiently small switching period T, it is possible to accurately estimate $\mathbf{y}(t)$ by $\bar{\mathbf{y}}(t)+\mathbf{\Psi}_y$. $\bar{\mathbf{y}}(t)$ is the output of a time-invariant differential equation, and $\mathbf{\Psi}_y$ is a function of known variables. Hence, the addition of $\bar{\mathbf{y}}(t)$ and $\mathbf{\Psi}_y$ is computationally quicker than numerical integrations of fast switching PWM system (4) needed to compute $\mathbf{y}(t)$. These and other issues on computational efficiency of averaged equations over switching PWM systems can be found in [6]. In [6], envelope methods are used for simulation purposes and the envelope approximation is assumed triangular—based on a two-term approximation of a matrix exponent. The above theorem generalizes these assumptions by using formal KBM averaging methods [1], which permits the modeling of parasitics.

Conclusion 2) of the theorem shows that, for any time interval of length T, i.e., $t\in[t_1,t_1+T]$, the peak values of $\mathbf{y}(t)$ will not differ much from the corresponding envelope value at time t_1. As a result, envelope functions $\mathbf{y}_{\max}(t)$ and $\mathbf{y}_{\min}(t)$ can be viewed as moving averages of the maximum and minimum values of $\mathbf{y}(t)$, respectively. Conclusion 3) simply states that the theorem is valid on an infinite time interval when the averaged system is uniformly asymptotically stable.

B. Small-Signal Modeling

1) Problem Statement and Motivation: System (1) and (10) is time-invariant and it is possible to perform linearization and small-signal analysis. In this way, one can quantify the effects of inputs and disturbances on the minimum and maximum values of y_i using transfer function analysis. Such an approach is typically applied to the conventional averaged model (1) and (2) in order to characterize loop gains and input/output transfer functions. To understand the concept further, let us motivate the idea by discussing dc–dc converter applications.

Consider Fig. 1, which represents a general diagram of a multi-input multi-output power block of a dc–dc converter. The inputs $\mathbf{u}=[u_1\ u_2]^T=[v_{\text{in}}\ i_o]^T$ are the input voltage and output small-signal current. The outputs $\mathbf{y}=[y_1\ y_2]^T=[i_{\text{in}}\ v_o]^T$ are the input current and output voltage. The notation of upper case, e.g., U_1, denotes dc values and the notation of "~," e.g., $\tilde{u}_1$, denotes a small-signal ac perturbation. Therefore, in this notation $u_1=U_1+\tilde{u}_1$.

For time-invariant systems, this formulation allows performance to be judged via characteristics of transfer functions such as audio susceptibility ($=\tilde{v}_o(s)/\tilde{v}_{\text{in}}(s)$), input admittance ($=\tilde{i}_{\text{in}}(s)/\tilde{v}_{\text{in}}(s)$), output impedance ($=\tilde{v}_o(s)/\tilde{i}_o(s)$), current susceptibility ($=\tilde{i}_{\text{in}}(s)/\tilde{i}_o(s)$), and control loop ($=\tilde{v}_o(s)/\tilde{d}(s)$). For dc–dc converters, these transfer functions are derived from the averaged dynamics of the system.

In this paper, however, new small-signal transfer functions are introduced that are applicable to peak values of output signals $y_i(t)$. The need for quantification of the behavior of peak output signals is justified in Fig. 3, which represents experimental steady-state outputs of the boost converter in Fig. 2, with ESR. The lower trace in Fig. 3 is the output voltage, while the upper one shows the input inductor current. Since the outputs are periodic, they obtain maximum and minimum on each switching cycle. The goal of this subsection is to determine how input perturbations affect the maximum and minimum outputs. In general, it *cannot* be assumed that perturbations affect the peaks and the averaged outputs identically.

For example, suppose that there is a small-signal sinusoidal perturbation of the output current. Assuming the duty ratio d remains constant (open loop operation) the output voltage and output current will then look like Fig. 4 Under the assumption that the switching frequency is much faster than the frequency of the input perturbation, envelopes of the peak values of the output voltage become sinusoidal. As a result, it is possible to measure the amplitude and phase of the envelopes of the sinusoidal traces and create new transfer functions such as

$$\begin{aligned}
\text{maximum audio susceptibility} &\equiv \tilde{v}_{o\max}(s)/\tilde{v}_{\text{in}}(s)\\
\text{minimum audio susceptibility} &\equiv \tilde{v}_{o\min}(s)/\tilde{v}_{\text{in}}(s)\\
\text{maximum input admittance} &\equiv \tilde{i}_{\text{in}\max}(s)/\tilde{v}_{\text{in}}(s)\\
\text{minimum input admittance} &\equiv \tilde{i}_{\text{in}\min}(s)/\tilde{v}_{\text{in}}(s)\\
\text{maximum output impedance} &\equiv \tilde{v}_{o\max}(s)/\tilde{i}_o(s)\\
\text{minimum output impedance} &\equiv \tilde{v}_{o\min}(s)/\tilde{i}_o(s)\\
\text{maximum current susceptibility} &\equiv \tilde{i}_{\text{in}\max}(s)/\tilde{i}_o(s)\\
\text{minimum current susceptibility} &\equiv \tilde{i}_{\text{in}\min}(s)/\tilde{i}_o(s)\\
\text{maximum control loop} &\equiv \tilde{v}_{o\max}(s)/\tilde{d}(s)\\
\text{minimum control loop} &\equiv \tilde{v}_{o\min}(s)/\tilde{d}(s).
\end{aligned}$$

These new transfer functions represent a measure of the change in the maximum and minimum outputs when there is a small

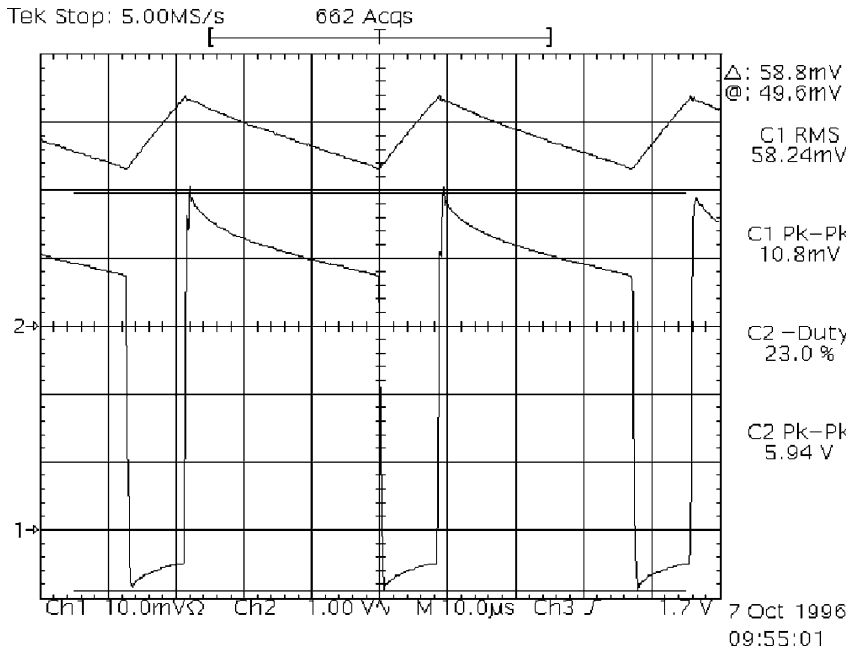

Fig. 3. Steady-state output signals for the boost converter.

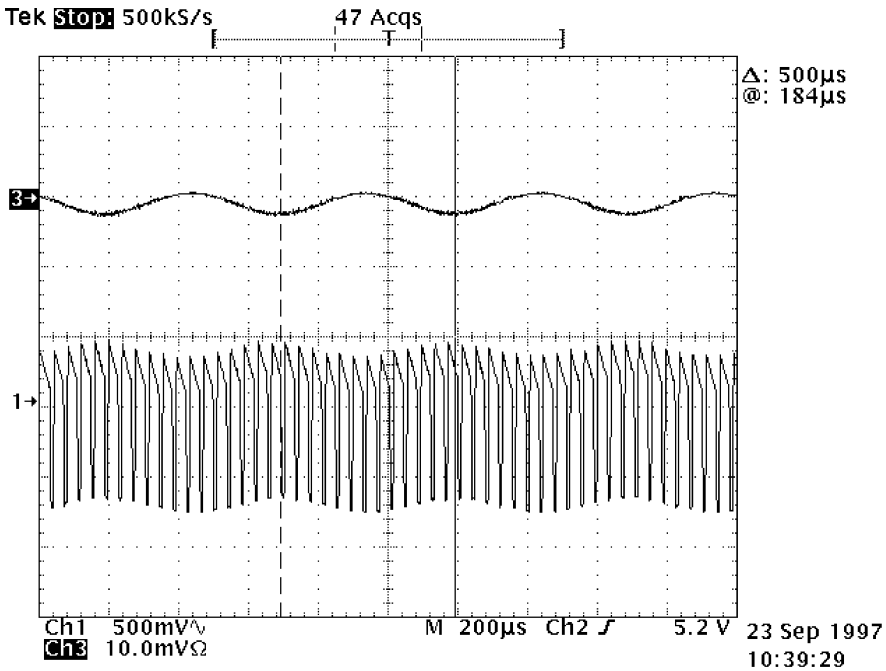

Fig. 4. Perturbed input and output signals for the boost converter.

signal perturbation in the input source (the denominator term of each transfer function).

The usefulness of these transfer functions depends on the application. For example, for output voltage feedback, the work of [8] demonstrates that the minimum or maximum output voltage, not the averaged output voltage, determines the duty ratio. Hence, the minimum control loop transfer function might influence control loop design. In another application, the designer may be concerned with the effect an output current disturbance has on the maximum value of the input current. This is an issue when selecting the power switches on the input side of a dc–dc converter. In this case, the maximum current susceptibility becomes important. Similarly, a designer of distributed power supplies is probably more concerned with the maximum or minimum output impedance than output impedance (in the classical averaged sense), since stability matching conditions are derived in terms of worst case scenarios [20].

2) Algorithm: Continuing with the previous algorithm, we present the following step.

Step 6: Linearize and Obtain Small-Signal Transfer Functions: An advantage of using continuous time models instead of discrete time models is that it permits analysis of small-signal

transfer functions. The classical approach is to first linearize the averaged equations in **Step 2** by letting $\bar{\mathbf{x}} = \tilde{\mathbf{x}} + \mathbf{X}$, $d = \tilde{d} + D$ and $\mathbf{u} = \tilde{\mathbf{u}} + \mathbf{U}$, $\bar{\mathbf{y}} = \tilde{\mathbf{y}} + \mathbf{Y}$, and neglecting higher order terms, where $\mathbf{X}$, D, $\mathbf{U}$, and $\mathbf{Y}$ denote steady-state values of (1) and (2). Then the small-signal linearization becomes

$$\begin{aligned}\dot{\tilde{\mathbf{x}}} &= \mathbf{A}(D)\tilde{\mathbf{x}} + \mathbf{B}(D)\tilde{\mathbf{u}} + \mathbf{E}(\mathbf{X},\mathbf{U})\tilde{d} \\ \tilde{\mathbf{y}} &= \mathbf{C}(D)\tilde{\mathbf{x}} + [(\mathbf{C}_1 - \mathbf{C}_2)\mathbf{X} + \mathbf{F}(D)\mathbf{U}]\,\tilde{d} \end{aligned} \tag{18}$$

where $\mathbf{E}(\mathbf{X},\mathbf{U}) = [(\mathbf{A}_1 - \mathbf{A}_2)\mathbf{X} + (\mathbf{B}_1 - \mathbf{B}_2)\mathbf{U} + \mathbf{G}_1 - \mathbf{G}_2]$ and $\mathbf{A}(D)$, $\mathbf{B}(D)$, $\mathbf{C}(D)$, and $\mathbf{F}(D)$ are as defined in **Step 2**, with $d = D$.

Laplace transforms can be taken to obtain small-signal performance transfer functions from the following equation:

$$\begin{aligned}\tilde{\mathbf{y}}(s) = \mathbf{C}(D)\,[s\mathbf{I} - \mathbf{A}(D)]^{-1}\left[\mathbf{B}(D)\tilde{\mathbf{u}}(s) + \mathbf{E}(\mathbf{X},\mathbf{U})\tilde{d}(s)\right] \\ + [(\mathbf{C}_1 - \mathbf{C}_2)\mathbf{X} + \mathbf{F}(D)\mathbf{U}]\,\tilde{d}(s). \end{aligned} \tag{19}$$

This is the classical result given in [13] and [12] that allows a designer to analyze the system's small-signal *averaged* transfer functions.

However, the above procedure only permits modeling of the averaged output. Using the information in **Steps 4** and **5**, it is possible to model the peak variations in the voltage by frequency-domain techniques, also. For example, linearizing $\mathbf{y}_{\max}$ from **Step 5** will lead to

$$\tilde{\mathbf{y}}_{\max} = \tilde{\mathbf{y}} + \frac{\partial \boldsymbol{\Psi}_{y_{\max}}}{\partial \bar{\mathbf{x}}}\tilde{\mathbf{x}} + \frac{\partial \boldsymbol{\Psi}_{y_{\max}}}{\partial d}\tilde{\mathbf{d}} + \frac{\partial \boldsymbol{\Psi}_{y_{\max}}}{\partial \mathbf{u}}\tilde{\mathbf{u}} \tag{20}$$

where each partial derivative is evaluated at steady-state values, i.e., $\partial \boldsymbol{\Psi}_{y_{\max}}/\partial \mathbf{u} = \partial \boldsymbol{\Psi}_{y_{\max}}(\mathbf{X}, D, \mathbf{U})/\partial \mathbf{u}$, etc.

Now it is possible to take Laplace transforms to derive transfer functions such as *maximum* audio-susceptibility, *maximum* output impedance, *maximum* input admittance, or *maximum* output current susceptibility from (set $\tilde{d} = 0$)

$$\begin{aligned}\tilde{\mathbf{y}}_{\max}(s) = \left[\mathbf{C}(D) + \frac{\partial \boldsymbol{\Psi}_{y_{\max}}}{\partial \bar{\mathbf{x}}}\right][s\mathbf{I} - \mathbf{A}(D)]^{-1}\mathbf{B}(D)\tilde{\mathbf{u}}(s) \\ + \frac{\partial \boldsymbol{\Psi}_{y_{\max}}}{\partial \mathbf{u}}\tilde{\mathbf{u}}(s) \end{aligned} \tag{21}$$

and pertaining *minimum* transfer functions from

$$\begin{aligned}\tilde{\mathbf{y}}_{\min}(s) = \left[\mathbf{C}(D) + \frac{\partial \boldsymbol{\Psi}_{y_{\min}}}{\partial \bar{\mathbf{x}}}\right][s\mathbf{I} - \mathbf{A}(D)]^{-1}\mathbf{B}(D)\tilde{\mathbf{u}}(s) \\ + \frac{\partial \boldsymbol{\Psi}_{y_{\min}}}{\partial \mathbf{u}}\tilde{\mathbf{u}}(s). \end{aligned} \tag{22}$$

Likewise, control transfer function for *maximum* and *minimum* peak output values are (set $\tilde{u} = 0$)

$$\begin{aligned}\tilde{\mathbf{y}}_{\max}(s) = \left[\mathbf{C}(D) + \frac{\partial \boldsymbol{\Psi}_{y_{\max}}}{\partial \bar{\mathbf{x}}}\right][s\mathbf{I} - \mathbf{A}(D)]^{-1} \cdot \mathbf{E}(\mathbf{X},\mathbf{U})\tilde{d}(s) \\ + \left[\frac{\partial \boldsymbol{\Psi}_{y_{\max}}}{\partial d} + (\mathbf{C}_1 - \mathbf{C}_2)\mathbf{X} + \mathbf{F}(D)\mathbf{U}\right]\tilde{d}(s) \end{aligned} \tag{23}$$

$$\begin{aligned}\tilde{\mathbf{y}}_{\min}(s) = \left[\mathbf{C}(D) + \frac{\partial \boldsymbol{\Psi}_{y_{\min}}}{\partial \bar{\mathbf{x}}}\right][s\mathbf{I} - \mathbf{A}(D)]^{-1} \cdot \mathbf{E}(\mathbf{X},\mathbf{U})\tilde{d}(s) \\ + \left[\frac{\partial \boldsymbol{\Psi}_{y_{\min}}}{\partial d} + (\mathbf{C}_1 - \mathbf{C}_2)\mathbf{X} + \mathbf{F}(D)\mathbf{U}\right]\tilde{d}(s). \end{aligned} \tag{24}$$

As a result, it is now possible to obtain small-signal transfer functions for the peak signal values in dc–dc converters. This gives the designer insight on how disturbances will affect the maximum and minimum outputs of a system.

It should be noted that the new minimum and maximum transfer functions differ from the classical transfer functions in the location of plant zeros and the dc gain. The location of the poles, though, remain the same. This is due to the fact that the state differential equations for the envelope system is the same as that for the averaged system. Only the output equation has changed.

III. Open-Loop Experiments and Simulation Results for Boost Converter

Consider the PWM voltage mode control boost converter in Fig. 2 which is similar to the classical benchmark problem described by [10]. A snubber is placed across the power transistor, but (since its time constant is over ten times the natural time constant) is not modeled, and the parasitics in the diode are assumed to be a voltage plus resistor model. Additional ESR has been added, denoted by R_T, in order to illustrate the effectiveness of the modeling technique and to demonstrate the effect of high ESR. Let $\mathbf{x} = [i_L\ v_C]^T$ and $\mathbf{u} = [u_1\ u_2]^T = [v_{\text{in}}\ i_o]^T$ and assume that $\mathbf{y} = [i_{\text{in}}\ v_o]^T$, the input current and the output voltage across the load. In this case, we have

$$\mathbf{A}_1 = \begin{bmatrix} -\frac{R_L + R_Q}{L} & 0 \\ 0 & -\frac{1}{C(R + R_C + R_T)} \end{bmatrix}$$

$$\mathbf{A}_2 = \begin{bmatrix} -\frac{R_L + R_D}{L} - \frac{R(R_C + R_T)}{L(R + R_C + R_T)} & -\frac{R}{L(R + R_C + R_T)} \\ \frac{R}{C(R + R_C + R_T)} & -\frac{1}{C(R + R_C + R_T)} \end{bmatrix}$$

$$\mathbf{B}_1 = \begin{bmatrix} \frac{1}{L} & 0 \\ 0 & \frac{R}{C(R + R_C + R_T)} \end{bmatrix}$$

$$\mathbf{B}_2 = \begin{bmatrix} \frac{1}{L} & -\frac{R(R_C + R_T)}{L(R + R_C + R_T)} \\ 0 & \frac{R}{C(R + R_C + R_T)} \end{bmatrix}$$

$$\mathbf{G}_1 = \begin{bmatrix} -\frac{V_Q}{L} \\ 0 \end{bmatrix}$$

$$\mathbf{G}_2 = \begin{bmatrix} -\frac{V_D}{L} \\ 0 \end{bmatrix}$$

$$\mathbf{C}_1 = \begin{bmatrix} 1 & 0 \\ 0 & \frac{R}{R + R_C + R_T} \end{bmatrix}$$

$$\mathbf{C}_2 = \begin{bmatrix} 1 & 0 \\ \frac{R(R_C + R_T)}{R + R_C + R_T} & \frac{R}{R + R_C + R_T} \end{bmatrix}$$

$$\mathbf{F}_1 = \mathbf{F}_2 = \begin{bmatrix} 0 & 0 \\ 0 & \frac{R(R_C + R_T)}{R + R_C + R_T} \end{bmatrix}.$$

For the purposes of illustration, the dc steady-state duty ratio is selected as $D = 0.23$, and switching frequency, $f_S = 1/T_S$, is set to 25 kHz. We then have steady-state average values of $Y_2 = V_o = 12.0363$ V, $X_1 = I_L = 1.231$ A, and $X_2 = V_C = 12.0363$ V. For the used MOSFET, IRF541, experiments show that forward voltage drop can be accurately modeled with only a resistor, i.e., $V_Q = 0$.

A. Large-Signal and Steady-State Accuracy

Application of the above algorithm is directly achieved by using the above matrices and following the step-by-step procedure. Using (3) and (7), it is possible to explicitely solve for the output ripple.

When the transistor is on, (7) gives

$$\Psi_{y_2\text{on}} = -\frac{R^2\bar{x}_1}{C(R+R_C+R_T)^2}\left[(1-d)t+\frac{T}{2}d(d-1)\right] - \frac{R(R_C+R_T)\bar{x}_1}{R+R_C+R_T}(1-d), 0<t\bmod(T)<dT. \quad (25)$$

When the transistor is off, however, the ripple of the inductor current recharges the output filter capacitor in order to maintain constant output voltage. On average, the inductor current does succeed in keeping constant output voltage, but, in the off state, it also contributes to the output voltage ripple jump. In this case, (7) gives

$$\Psi_{y_2\text{off}} = \left\{\frac{R(R_C+R_T)}{R+R_C+R_T}\cdot\left[\frac{(R_D-R_Q)\bar{x}_1}{L}+\frac{R(R_C+R_T)\bar{x}_1}{L(R+R_C+R_T)} + \frac{R\bar{x}_2}{L(R+R_C+R_T)}\right] - \frac{R^2\bar{x}_1}{C(R+R_C+R_T)^2} + \frac{R(R_C+R_T)V_D}{L(R+R_C+R_T)}\right\}\left[(-d)t+\frac{T}{2}d(d+1)\right] - \frac{R(R_C+R_T)}{R+R_C+R_T}\bar{x}_1(-d), dT<t\bmod(T)<T. \quad (26)$$

The output voltage ripple is discontinuous and has significant peak to peak variations. The averaged output voltage, as predicted by **Step 2** (classical methods), does not reflect these variations and is equal to a constant. Fig. 5(a) gives theoretical prediction of $v_o(t)$ in the steady state and corresponds well to the experimental plot of Fig. 6. It should be noted here that the discontinuities are due to the ESR and cannot be predicted using the techniques of [7], [8], and [17]. Also, it is interesting to notice that the inductor resistance R_L does not directly appear in the ripple, although it affects the ripple implicitly: R_L changes the (transient and steady-state) values of $\bar{x}_1$ and $\bar{x}_2$, since it adds additional power loss to the circuit. This can be predicted through the averaged (1). Thus, the value of R_L will implicitly influence the ripple Ψ_{y_2} in this example through $\bar{x}_1$ and $\bar{x}_2$.

Theoretical predictions of maximum and minimum steady-state values of $v_o(t)$ are given as 12.44 and 11.34 V, respectively. These values were experimentally determined to be 12.36 and 11.10 V, respectively, which represents 0.65% and 2.16% error, respectively. The average value of the output voltage is theoretically predicted to be 11.95 V, while experiments show 11.852 V, which is 0.82% error.

$y_{\max/\min}(t)$ can be derived from (10). In the boost converter, $\Psi_{y_{2\min}}$ as defined in (8) occurs at $t_{2\max} = c_2T^+ = dT^+$, which is the instant after the discontinuous jump of current through the diode. Similarly, we have $t_{2\min} = dT^-$ (the time when the output voltage is at its minimum. Specifically, (10) leads to

$$\Psi_{y_{2\min}} = -\frac{R^2\bar{x}_1}{C(R+R_C+R_T)^2}\left[\frac{T}{2}d(1-d)\right] - \frac{R(R_C+R_T)\bar{x}_1}{R+R_C+R_T}(1-d) \quad (27)$$

Likewise

$$\Psi_{y_{2\max}} = \left\{\frac{R(R_C+R_T)}{R+R_C+R_T}\cdot\left[\frac{(R_D-R_Q)\bar{x}_1}{L}+\frac{R(R_C+R_T)\bar{x}_1}{L(R+R_C+R_T)} + \frac{R\bar{x}_2}{L(R+R_C+R_T)}\right] - \frac{R^2\bar{x}_1}{C(R+R_C+R_T)^2} + \frac{R(R_C+R_T)V_D}{L(R+R_C+R_T)}\right\}\left[\frac{T}{2}d(1-d)\right] - \frac{R(R_C+R_T)}{R+R_C+R_T}\bar{x}_1(-d). \quad (28)$$

Fig. 5(a) shows how $y_{2\min} = \bar{y}_2 + \Psi_{y_{2\min}}$ and $y_{2\max} = \bar{y}_2 + \Psi_{y_{2\max}}$ bound the output voltage y_2. This figure is given for steady state. On the other hand, the large-signal modeling procedure is accurate in transient analysis, as previous theorems indicate. Calculations and simulations are plotted in Fig. 5(b) for input current during transient start-up. Notice that $y_{1\max}$ accurately predicts the maximum envelope of the original switching output, given by (5). A similar statement can be made for the minimum values. Hence, on a cycle-by-cycle basis, the new models are able to predict maximum and minimum transient output values with accuracy. Hence, the models are accurate for both transient and steady-state analysis.

Analysis can also be performed in a similar manner for the input current ripple Ψ_{y_1}. However, notice that, for a boost converter, the input current y_1 is equal to the inductor current x_1. Thus, $\Psi_{y_1} = \Psi_{x_1}$, which can also be derived directly from (7) using the values for the matrices provided above. Thus, known state-ripple estimates can be applied to calculate Ψ_{y_1} (see [7] and [8] for more details of this calculation).

B. Small-Signal Experimental and Simulation Results

Consider once again the boost converter as shown in Fig. 2. As Fig. 2 shows, a small-signal input voltage source with variable frequency has been injected (through a power transformer) to the input. All circuit values remain the same as in Fig. 2 while the small-signal input current source $\tilde{u}_2(t)$ is disconnected.

Audio Susceptibility for Boost Converter: The results of the measurements of audio susceptibility were compared with their pertaining theoretical predictions in (19), (21), and (22) for *averaged* audio susceptibility, *maximum* audio susceptibility, and *minimum* audio susceptibility, respectively. Fig. 7 shows the differences between them.

Now consider (21), with $u_2 = 0$, which is used to derive the *maximum* audio susceptibility. Notice that this new transfer function differs from the averaged audio susceptibility by including new terms $\partial\mathbf{\Psi}_{y_{\max}}/\partial\bar{\mathbf{x}}$ and $\partial\mathbf{\Psi}_{y_{\max}}/\partial\mathbf{u}$. Using (7), it is possible to explicitly calculate $\partial\mathbf{\Psi}_{y_{\max}}/\partial\bar{\mathbf{x}} = \mathbf{C}_2(\mathbf{A}_1-\mathbf{A}_2)(T/2)D(1-D)-(\mathbf{C}_1-\mathbf{C}_2)D$. It is interesting to note that, for a boost converter, the term $\partial\mathbf{\Psi}_{y_{\max}}/\partial u_1 = \mathbf{C}_2(\mathbf{B}_1-\mathbf{B}_2)(T/2)D(1-D)[1\ 0]^T = 0$.

The calculated transfer functions for the boost converter in Fig. 2 (with $R_T = 0.75\ \Omega$) are

$$\frac{\tilde{y}_2(s)}{\tilde{u}_1(s)} = \frac{2.692\times10^3(s+545.59)}{s^2+3.0363\times10^3 s+1.1603\times10^6}$$

$$\frac{\tilde{y}_{2\max}(s)}{\tilde{u}_1(s)} = \frac{3.5335\times10^3(s+429.4326)}{s^2+3.0363\times10^3 s+1.1603\times10^6}$$

$$\frac{\tilde{y}_{2\min}(s)}{\tilde{u}_1(s)} = \frac{6.3684(2.1735\times10^5-s)}{s^2+3.0363\times10^3 s+1.1603\times10^6}.$$

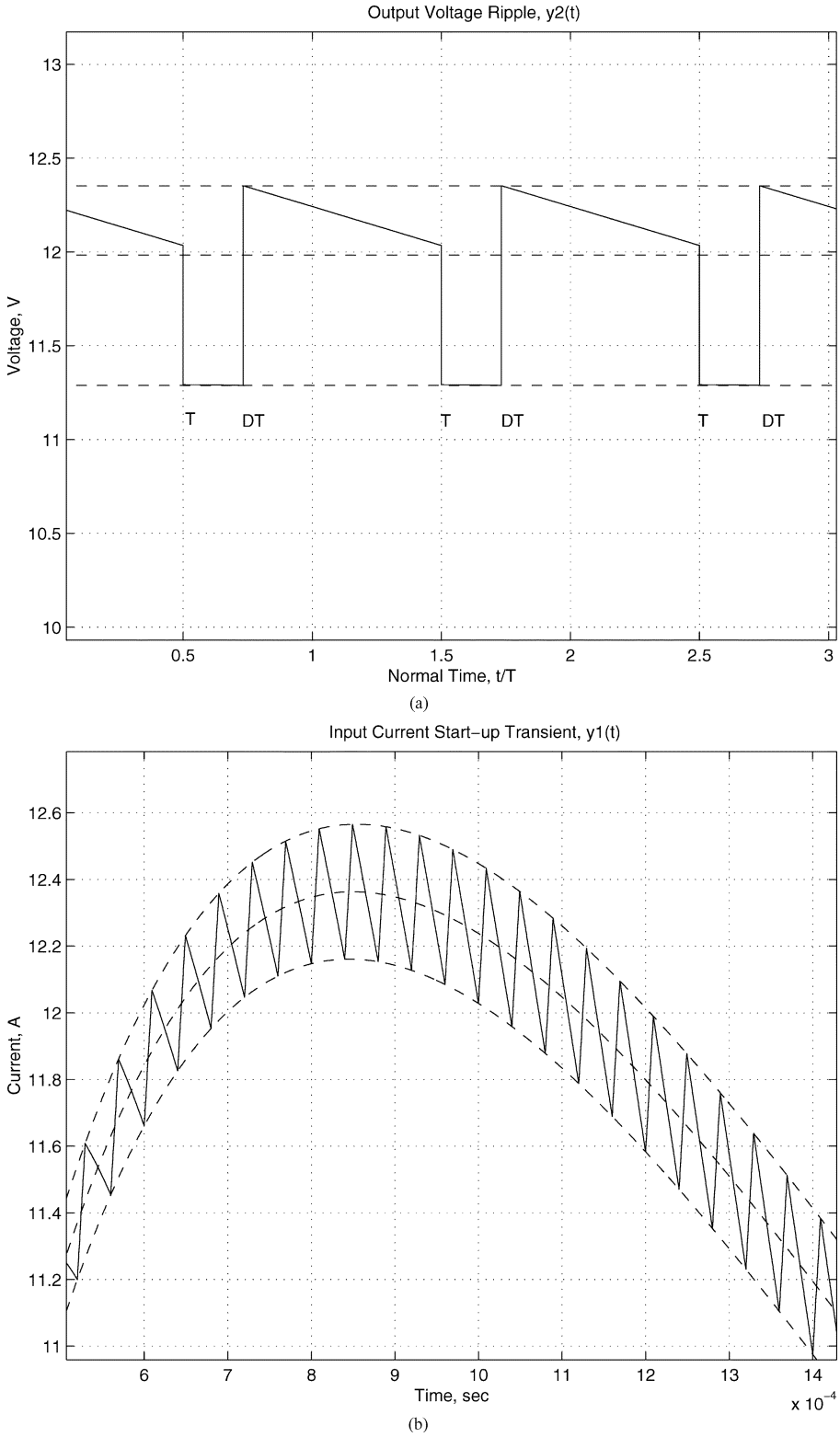

Fig. 5. (a) Theoretically predicted steady-state output voltage and (b) transient of the input current ripple waveform, as predicted in Step 4. Top, middle, and bottom broken lines represent $y_{i\ \max}(t)$, $y_{i\ \mathrm{avg}}(t)$, and $y_{i\ \min}(t)$, i $= 1, 2$ respectively, as predicted in Step 5.

The differences in *maximum* audio susceptibility compared with the *averaged* audio susceptibility (29) can be seen by comparing the explicit transfer functions in the example. *Maximum* audio susceptibility has a displaced zero (closer to the origin) and a small increase in dc gain. *Minimum* audio susceptibility even has a zero in the (far) right-hand plane and the lowest dc gain. The location of the poles is the same whether considering the *maximum*, *minimum*, or *averaged* audio susceptibility. The interpretation of the results, however, is that small-signal input voltage disturbances are magnified more for maximum peak output voltage than for the averaged output and especially more than the minimum in

Fig. 6. Experimental steady-state output voltage ripple for boost benchmark converter.

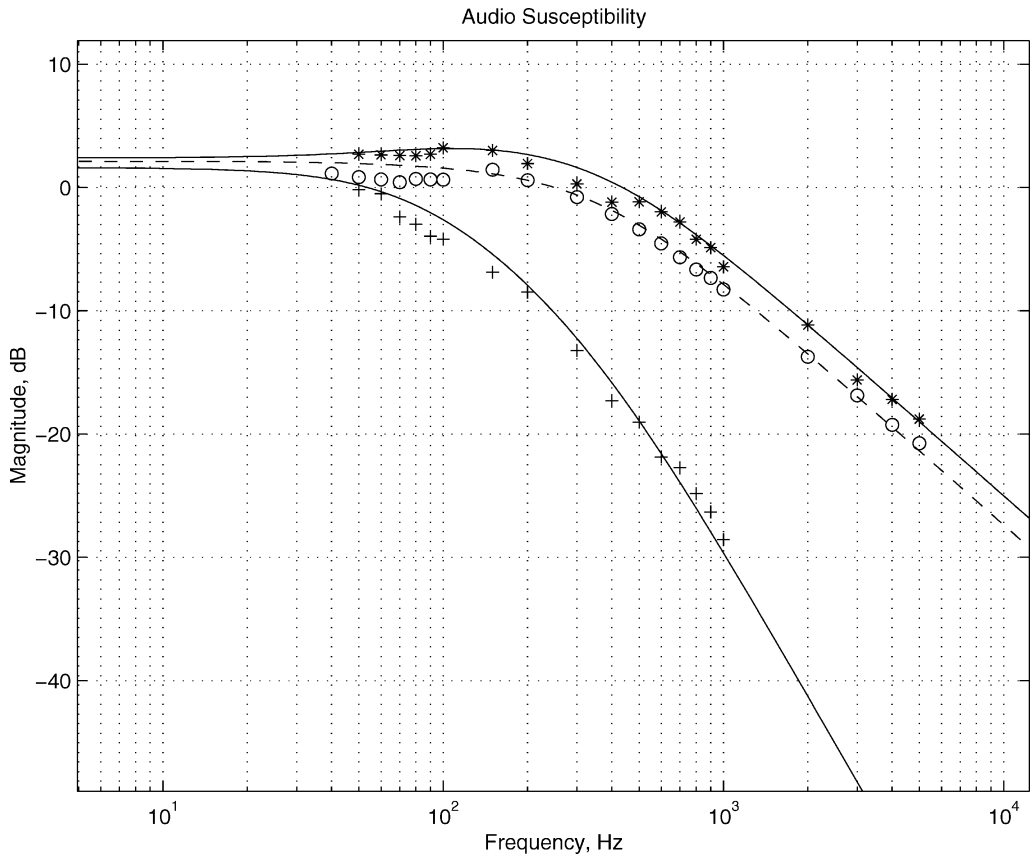

Fig. 7. Theoretically predicted audio susceptibility (avg., min., and max.) and experimental data points (min.: "+", max.: "*", and avg.: "o").

the roll-off region of the characteristic. This interpretation is justified since Fig. 7 clearly shows that the *maximum* audio susceptibility Bode plot is always greater than the *averaged* and *minimum* audio susceptibility Bode plots.

Input Admittance for Boost Converter: Now consider input current as an output variable and again small-signal input voltage source ($\tilde{u}_1(t)$ in Fig. 1) as a source of sinusoidal perturbation to the input. After modeling output ripples, input

admittance frequency characteristic emerges as an algebraic exercise using the previously described techniques. The results of the measurements and calculations of the input admittance frequency characteristic are shown in Fig. 8(a) and as follows:

$$\frac{\tilde{y}_1(s)}{\tilde{u}_1(s)} = \frac{4.786\,98 \times 10^4 (s + 31.38)}{s^2 + 3.0363 \times 10^3 s + 1.1603 \times 10^6}$$
$$\frac{\tilde{y}_{1\max}(s)}{\tilde{u}_1(s)} = \frac{4.845\,45 \times 10^4 (s + 36.22)}{s^2 + 3.0363 \times 10^3 s + 1.1603 \times 10^6}$$
$$\frac{\tilde{y}_{1\min}(s)}{\tilde{u}_1(s)} = \frac{4.728\,51 \times 10^4 (s + 26.41)}{s^2 + 3.0363 \times 10^3 s + 1.1603 \times 10^6}.$$

Theoretical models and experimental data verify almost no difference between the *averaged*, *maximum*, and *minimum* input admittance. Continuity of the input current plays a decisive role for this property of the boost converter, as opposed to the converter's discontinuous output voltage. In a buck derived converter, though, the input current is discontinuous and the results would not be the same.

Output Impedance for Boost Converter: For output impedance, it is the current source $\tilde{u}_2(t)$, in Fig. 2 (or Fig. 1), that is the source of small-signal perturbations. The sinusoidal input voltage source $\tilde{u}_1(t)$ is shorted. Measurements and modeling of the output impedance of the boost example are shown in Fig. 8(b). The calculated transfer functions are given as follows:

$$\frac{\tilde{y}_2(s)}{\tilde{u}_2(s)} = \frac{0.7304(s^2 + 1.1649 \times 10^3 s + 3.3786 \times 10^5)}{s^2 + 3.0363 \times 10^3 s + 1.1603 \times 10^6}$$
$$\frac{\tilde{y}_{2\max}(s)}{\tilde{u}_2(s)} = \frac{0.7395(s^2 + 550.3902 s + 2.6426 \times 10^3)}{s^2 + 3.0363 \times 10^3 s + 1.1603 \times 10^6}$$
$$\frac{\tilde{y}_{2\min}(s)}{\tilde{u}_2(s)} = \frac{0.7304(s^2 + 3.2429 \times 10^3 s + 3.3786 \times 10^5)}{s^2 + 3.0363 \times 10^3 s + 1.1603 \times 10^6}.$$

Minimum, *averaged*, and *maximum* output impedance distinguish themselves from each other in the low-frequency range. *Minimum* output impedance is almost constant since this frequency characteristic has almost overlapping zeros and poles. This implies that the minimum peak output voltage values perturbed by the small-signal current source are less attenuated, in the low-frequency range, than averaged output voltage and maximum peak output voltage. Implications of this fact on distributed power systems [20] remains an interesting future research topic.

Control Loop for Boost Converter: Control-loop frequency characteristic measurements and modeling results (19), (23), and (24), for the boost converter, are compared and shown in Fig. 9. The calculated transfer functions are given as follows:

$$\frac{\tilde{y}_2(s)}{\tilde{d}(s)} = \frac{-0.8992(s^2 - 3.5257 \times 10^4 s - 1.9533 \times 10^7)}{s^2 + 3.0363 \times 10^3 s + 1.1603 \times 10^6}$$
$$\frac{\tilde{y}_{2\max}(s)}{\tilde{d}(s)} = \frac{0.4844(s^2 + 9.6598 \times 10^4 s + 4.1321 \times 10^7)}{s^2 + 3.0363 \times 10^3 s + 1.1603 \times 10^6}$$
$$\frac{\tilde{y}_{2\min}(s)}{\tilde{d}(s)} = \frac{-0.0050(s^2 + 1.1201 \times 10^5 s - 3.3086 \times 10^9)}{s^2 + 3.0363 \times 10^3 s + 1.1603 \times 10^6}.$$

Source of the small-signal perturbation is in the duty ratio, d. Magnitude of the *minimum* control loop rolls off faster than the *average* or the *maximum* loop. This is due to the fact that the minimum control loop gain has a right half-plane zero around 3.9 kHz, whereas the other two control-to-output transfer functions have a zero near the plant pole at 70 Hz.

Remark 3: The new theoretical models predict the experimental "*peak*" frequency characteristics data. There is some error at certain frequencies, as demonstrated in presented experimental data. Since there is an interest in instantaneous values of switching periodic output signals most of the data has to be gathered "point by point." Modern-day oscilloscopes do not offer features that will measure periodic perturbation of the peak values at the frequencies sufficiently small in respect to switching frequency. This leads to an error contributed by insufficient resolution of the scope. Modeling error may also be caused by the inductive characteristic of the variable resistor load in our experiments, not included in model. Additionally, there are errors in using a voltage plus resistance model for the diode and other nonlinearities that have not been modeled.

Finally, it should be noted that the above experiments are measured for one particular operating point, i.e., for fixed D and $\mathbf{X}$. Different operating points may lead to different interpretations and conclusions for the new small signal transfer functions.

IV. Further Models and Simulations of a Closed-Loop Boost Converter

Although this paper has focused on modeling, and experiments are based on open-loop transfer functions, it is also possible to discuss issues in closed-loop performance. It has been noted in [8] that in boost converters the switching time occurs when the output voltage is at its minimum, i.e., $t = DT^{-}\mathrm{mod}T$. This leads to the question in voltage mode control of dc–dc converters as to whether we are actually feeding back $v_0(t)$ or are feeding back $v_{0\min}(t)$. We suggest that a good controller design might consider both possibilities to assure proper performance.

For example, in voltage mode control for dc–dc converters, the controller has dynamic equations

$$\begin{aligned} \dot{\mathbf{x}}_\mathbf{c} &= \mathbf{A}_c \mathbf{x}_c + \mathbf{B}_c v_0 \\ d &= V_{\mathrm{ref}} - \mathbf{C}_c \mathbf{x}_c - \mathbf{F}_c v_0. \end{aligned} \tag{29}$$

Conventional averaging methods would simulate (1) and (2) together with the averaged controller

$$\begin{aligned} \dot{\bar{\mathbf{x}}}_\mathbf{c} &= \mathbf{A}_c \bar{\mathbf{x}}_c + \mathbf{B}_c \bar{v}_0 \\ d &= V_{\mathrm{ref}} - \mathbf{C}_c \bar{x}_c - \mathbf{F}_c \bar{v}_0 \end{aligned} \tag{30}$$

where we make the assumption that $d = \bar{d}$. Then standard control design methods such as in [12] are used.

Suppose, though, the dc–dc converter is a Boost converter and is known to have ripple. The switching instant occurs when $v_0(t)$ is at its minimum. In fact, the function $h(d(\cdot, v_0) - \mathrm{tri}(t,T))$ in (4) is equal to $h(d(\cdot, v_{0\min}) - \mathrm{tri}(t,T))$. This is because h is either 0 or 1 and the switching time of the discontinuity depends only on the values of the states and outputs at $t = dT^{-}\mathrm{mod}T$. So another way to view an approximation of closed-loop system (4), (5), and (29) is that we are controlling the minimum value of the output voltage—not the average value. If we view the control problem in this way, then we can create an averaged system that tracks the minimum

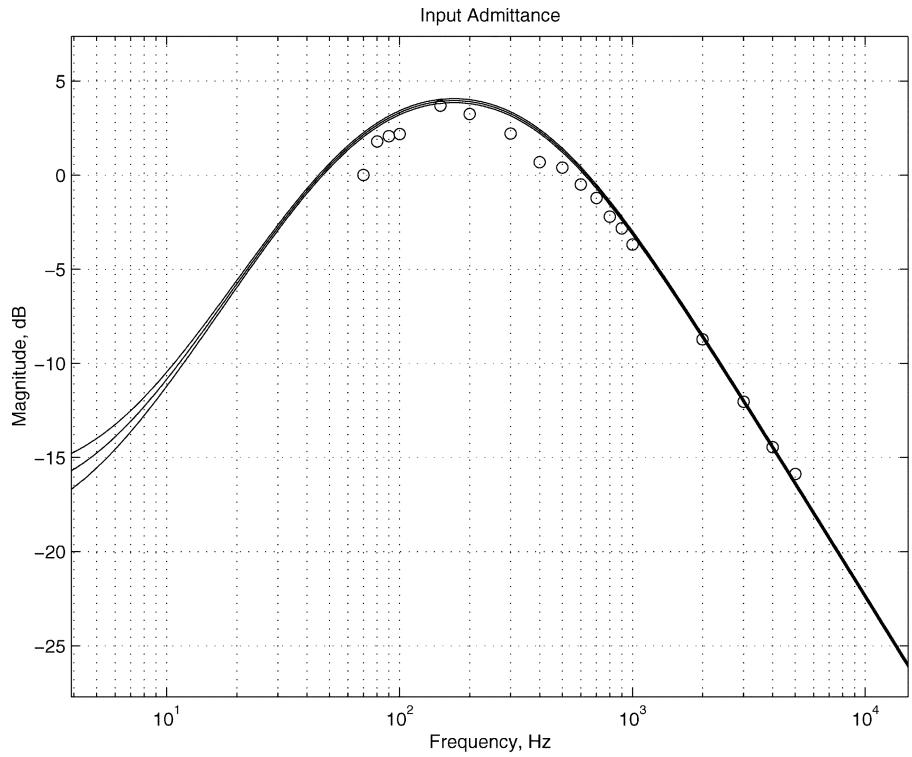

(a)

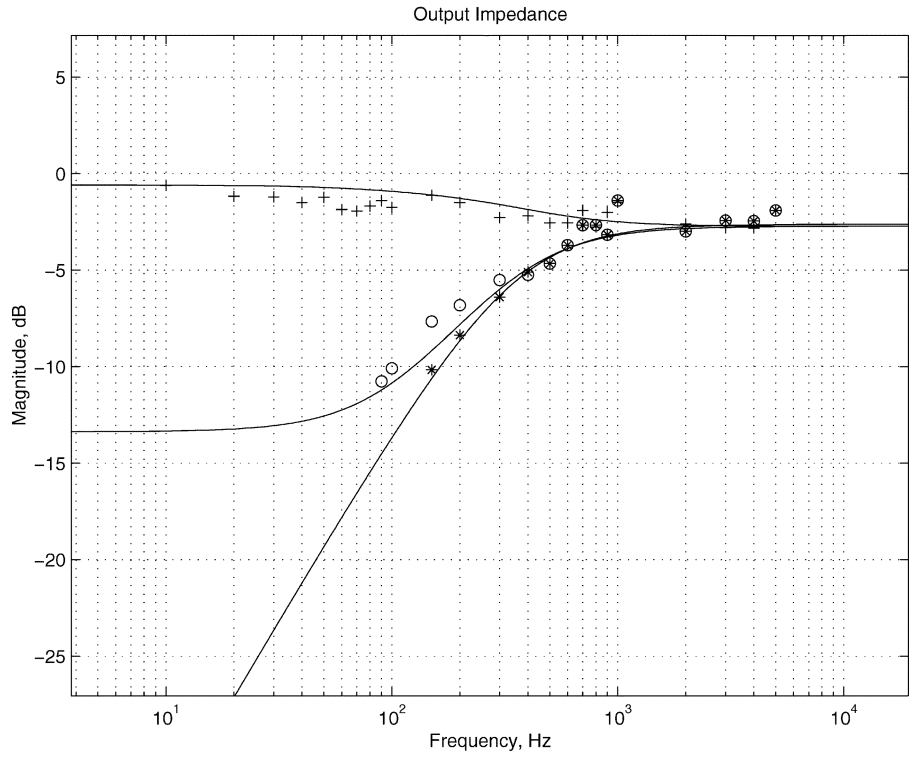

(b)

Fig. 8. (a) Theoretically predicted input admittance (avg., min., and max.) and experimental data points "o."(b) Theoretically predicted output impedance (avg., min. and max.) and experimental data points (min.: "+", max.: "*", and avg.: "o") .

value of v_0. That is, we might view an alternate/additional averaged control system as

$$\begin{aligned}\dot{\bar{\mathbf{x}}}_{\mathbf{c}} &= \mathbf{A}_c\bar{\mathbf{x}}_c + \mathbf{B}_c v_{0\,\min}\\ d &= V_{\text{ref}\,\min} - \mathbf{C}_c\bar{x}_c - \mathbf{F}_c v_{0\,\min}.\end{aligned} \tag{31}$$

Here, we are attempting to control the output $v_{0\,\min}$ by assuming that this is the quantity that is fed back into the controller for the averaged system. Notice that we use a new reference voltage in the controller. In order to obtain accurate large-signal simulations, it is necessary to reduce the reference voltage so that the

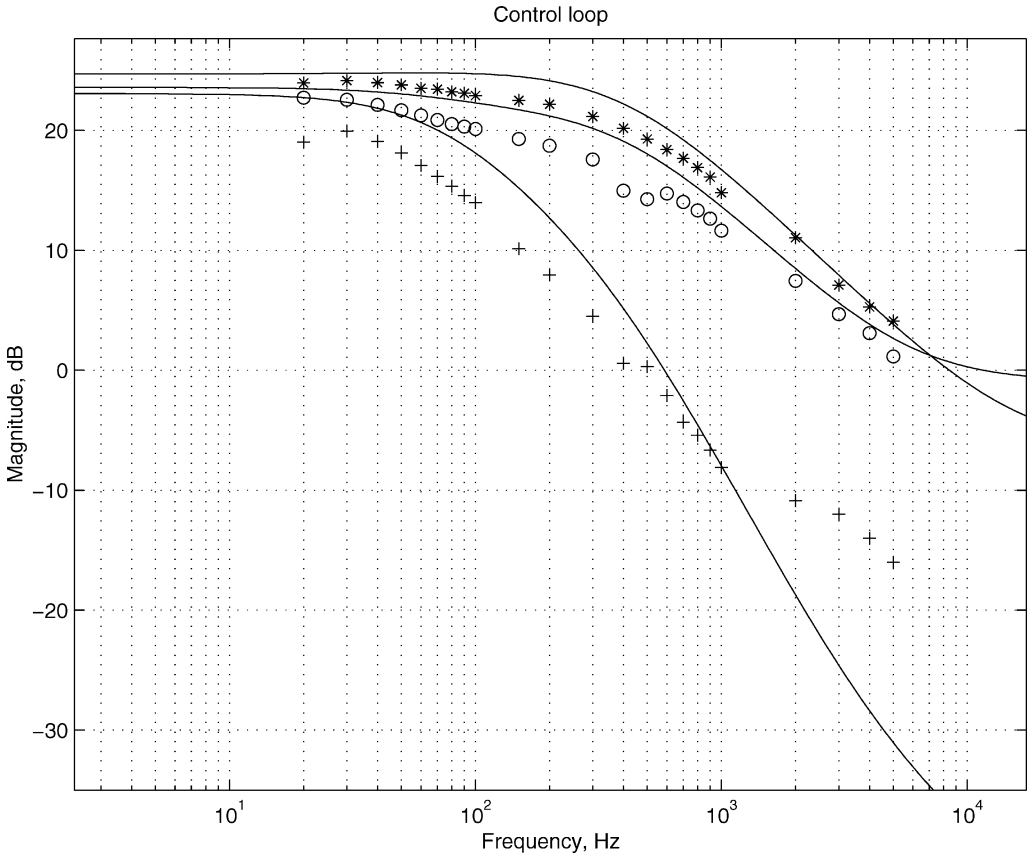

Fig. 9. Theoretically predicted control loop (avg., min., and max.) and experimental data points (min.: "+", max.: "*", and avg.: "o").

average output voltage is as desired. For the boost converter this leads to (1), (2),(10), and (31) representing a new closed-loop averaged model.

Therefore, for this boost converter with large output voltage ripple, we propose one possible control loop design procedure as follows:

1) Use conventional averaged models to design a controller. For voltage mode control, this is normally performed by using small-signal analysis for the loop gain. Hence, we design a controller, $G_C(s)$ so that the loop gain $G_C(s) \cdot (\tilde{v}_0(s)/\tilde{d}(s))$ has sufficient phase margin, gain margin, and crossover frequency. We select $V_{\rm ref}$ to obtain the desired average output steady-state value V_0.
2) Verify that the minimum loop gain $G_C(s) \cdot (\tilde{v}_{0\,\min}(s)/\tilde{d}(s))$ has sufficient phase margin, gain margin, and crossover frequency. For converters with small output voltage ripples, the average loop gain will be almost identical to the minimum loop gain. If not, repeat steps 1) and 2) until a desired controller is found. Then calculate a new $V_{ref\,\min}$ in (31) to give the desired minimum and averaged values for (1), (2), (10), and (31).
3) Simulate and test (1), (2), (10), and (31) under different line and load test conditions to verify performance. Verify that the large-signal transient behavior is satisfactory.
4) Simulate and test the conventional large signal average model (1), (2), and (29) under different line and load test conditions to verify performance. Verify that the large-signal transient behavior is satisfactory.
5) Once the above steps are complete, simulate the actual switching model for a few select line and load test conditions. These final simulations should verify that the envelopes in the previous simulation steps are accurate.

The above design procedure differs from conventional methods [12] by introducing two new steps [steps 2) and 3)] to assure proper performance of the minimum values of output voltage, i.e., assuring that the minimum loop gain has proper characteristics and the new minimum nonlinear averaged model behaves satisfactory. In fact, as we will now show, often the averaged model [(1), (2),(10), and (31)] is more accurate in predicting the actual behavior of the switching converter than conventional averaged models.

A. Example

Consider, once again, the benchmark boost converter with voltage mode control, this time with the proportional integral (PI) controller $G_C(s) = K_P + K_I/s$. We select $K_P = 0.098$ and $K_I = 11.46$. The controller has been designed so that performance of both control-loop gains are satisfactory. For example, the minimum and average loop gain have a phase margin of 109° and 135°, respectively, while achieving a crossover frequency of 456 and 1892 rad/s, respectively.

Fig. 10 simulates a large signal line variation from 10 to 9 V. The accuracy of using averaged controller (31) is apparent, while the conventional averaged model has inaccuracies, as the figure shows: specifically, it predicts that the change in average output voltage reduces down to (only) about 11.5 V before it eventually returns to its average steady state value of around

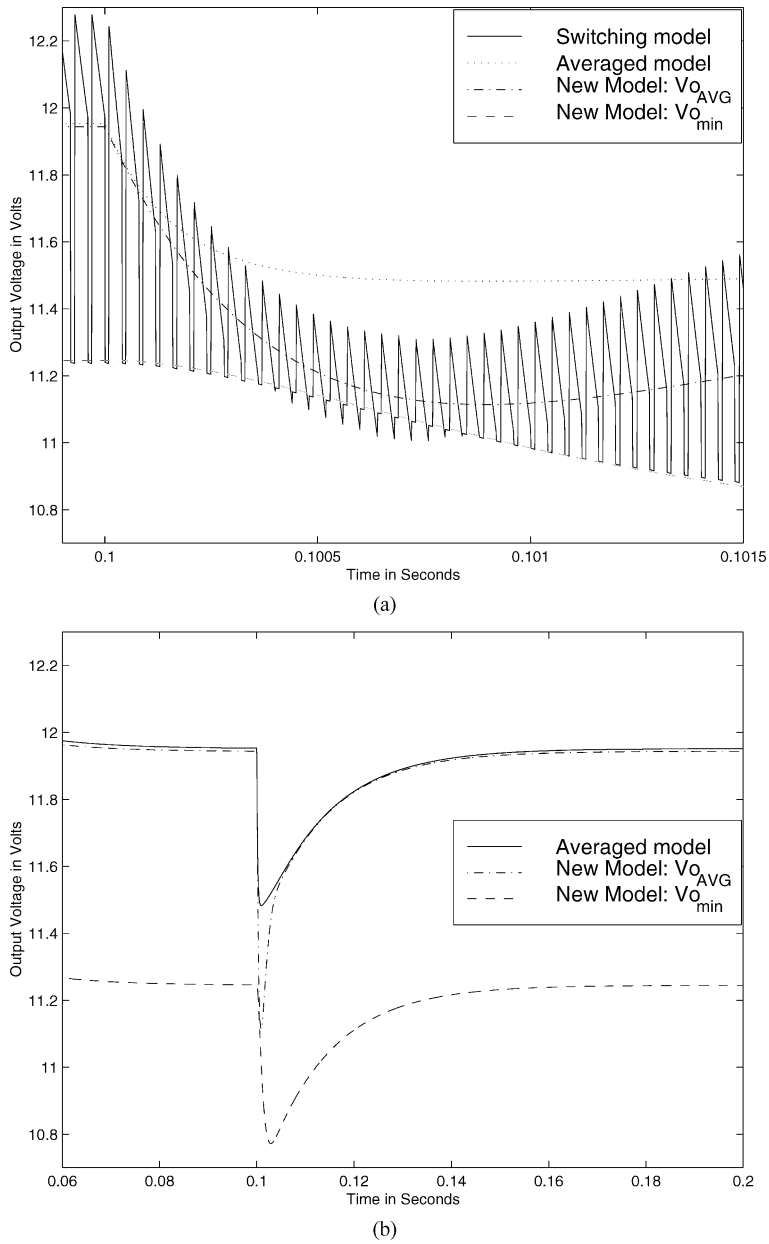

Fig. 10. (a) Output voltage of the three models. (b) Enlarged version of (a).

11.95 V. (The integration in the PI controller will always return the converter to its proper steady-state value provided stability and continuous conduction mode are guaranteed.) Notice, however, that using $v_{0\min}$ to determine d, as in (31), the transient behavior (average and minimum envelope) of $v_0(t)$ is accurately predicted. We see that the average value actually reaches a low value of 11.2 V while its minimum value goes as low as 11 V. This may be important when deciding whether the converter's performance remains acceptable. Since the crossover frequency of the minimum and average loop gain are comparable, the overall settling times are approximately the same. We remark that for the simulations $V_{\rm ref} = 0.23$ in (29) and $V_{\rm ref\,min} = 0.2164$ in (31).

Computation time for the new averaged models in our example is 1.25 min, while simulation time for the switching circuit is 34 min (in MATLAB on a Pentium III 600-MHz processor). This saving in simulation time is a main reason why line/load simulations are usually performed with averaged equations instead of the original switching equations. Another issue is the known convergence problems of simulating the fast switching PWM circuits. Using the envelope methods proposed, we have maintained peak value information that is normally lost in averaging.

V. Conclusion

New models have been derived for the maximum and minimum envelopes of output signals for dc–dc switching converters. The models are shown to be useful for both small-signal and large-signal analysis. It was shown that, when the ESR dominates, there can be a significant deviation in the averaged and peak output values. This can lead to errors in predicting

performance if conventional averaged models are used. The new models alleviate many of these errors. Rigorous mathematical justification has been presented to support the new models.

New small-signal transfer functions were introduced in order to aid the designer evaluate system response to disturbances. For a boost converter example, it was shown that *maximum* audio susceptibility has a wider bandwidth and a higher dc gain than the *averaged* and *minimum* audio-susceptibility. *Minimum* output impedance is amplified in the low-frequency region with respect to *averaged* and *maximum* output impedance. Experimental results verified the theoretical predictions. Future research will focus more on the implications of these transfer functions on control system design and on distributed power systems.

REFERENCES

[1] N. N. Bogoliubov and Y. A. Mitropolsky, *Asymptotic Methods in the Theory of Non-Linear Oscillations*. New York: Gordon and Breach, 1961.

[2] R. G. Bartle, *The Elements of Real Analysis*. New York: Wiley, 1976.

[3] K. C. Daly, "DC/DC converters ripple determination for switch mode," *Proc. Inst. Elect. Eng.*, vol. 129, pp. 229–234, Oct. 1982.

[4] A. F. Filippov, *Differential Equations with Discontinuous Righthand Sides*. Dordrecht, The Netherlands: Kluwer, 1988.

[5] P. T. Krein, J. Bentsman, R. M. Bass, and B. C. Lesieutre, "On the use of averaging for the analysis of power electronic systems," *IEEE Trans. Power Electron.*, vol. 5, pp. 182–190, Apr. 1990.

[6] J. White and S. Leeb, "An envelope-following approach to switching power converter simulation," *IEEE Trans. Power Electron.*, vol. 6, pp. 303–307, Apr. 1991.

[7] B. Lehman and R. M. Bass, "Extensions of averaging for power electronic systems," *IEEE Trans. Power Electron.*, vol. 11, pp. 542–553, July 1996.

[8] ——, "Switching frequency dependent averaged models for PWM DC-DC converters," *IEEE Trans. Power Electron.*, vol. 11, pp. 89–98, Jan. 1996.

[9] S. M. Meerkov, "Averaging of trajectories of slow dynamic systems," *Differential Equations*, vol. 9, no. 11, pp. 1239–1245, Jan. 1973.

[10] R. D. Middlebrook, "Modeling current-programmed buck and boost regulators," *IEEE Trans. Power Electron.*, vol. 4, pp. 36–52, Jan. 1989.

[11] R. D. Middlebrook and S. Ćuk, "A general unified approach to modeling switching converter power stages," in *IEEE Power Electronics Spec. Conf. Rec.*, 1976, pp. 18–34.

[12] D. M. Mitchell, *DC-DC Switching Regulator Analysis*. New York: McGraw-Hill, 1988.

[13] N. Mohan, T. M. Undeland, and W. P. Robbins, *Power Electronics: Converters, Applications, and Design*, 2nd ed. New York: Wiley, 1995.

[14] T. Sakharuk, B. Lehman, A. Stankovic, and G. Tadmor, "Effects of finite switching frequency and computational delay on PWM controlled servo drives," *IEEE Trans. Circuits Syst. I*, vol. 47, pp. 555–567, Apr. 2000.

[15] S. R. Sanders, J. M. Noworolski, X. Z. Liu, and G. C. Verghese, "Generalized averaging method for power conversion circuits," *IEEE Trans. Power Electron.*, vol. 6, pp. 251–259, Apr. 1991.

[16] V. Solo and X. Kong, *Adaptive Signal Processing Algorithms*. Englewood Cliffs, NJ: Prentice Hall, 1995.

[17] R. Tymerski and D. Li, "Extended ripple analysis of PWM DC-to-DC converters," *IEEE Trans. Power Electron.*, vol. 8, pp. 588–595, Oct. 1993.

[18] G. C. Verghese, C. A. Bruzos, and K. N. Mahabir, "Averaged and sampled-data models for current mode control: A reexamination," in *IEEE Power Electronics Spec. Conf. Rec.*, 1989, pp. 484–491.

[19] G. W. Wester and R. D. Middlebrook, "Low frequency characterization of switched Dc-to-Dc converters," in *IEEE Power Electronics Spec. Conf. Rec.*, 1972, pp. 9–20.

[20] C. M. Wildrick and F. C. Lee, "A method of defining the load impedance specification for a stable distributed power system," *IEEE Trans. Power Electron.*, vol. 10, pp. 280–285, May 1995.

Zoran Mihajlovic (S'91–M'98) received the Dipl. Ing. degree from the University of Zagreb, Zagreb, Croatia, and the M.S. degree from Northeastern University, Boston, MA, both in electrical engineering.

From 1994 to 1995, he worked on a 6-kW battery charger for an electric vehicle program at Power Control Systems, Torrance, CA. In 1995, he joined the Power Electronics and Motion Control Laboratory, Northeastern University, as a student and Research Assistant on design and generalization of dc–dc converters. Since 1998, he has been with the Plug-in Power Group (formerly Power Trends), Texas Instruments, Warrenville, IL, where he is designing power modules for point-of-load power architectures.

Brad Lehman (S'92–M'92) received the B.S. degree from the Georgia Institute of Technology, Atlanta, the M.S. degree from the University of Illinois at Champaign-Urbana, and the Ph.D. degree from the Georgia Institute of Technology in 1987, 1988, and 1992, respectively, all in electrical engineering.

He is presently an Associate Professor and Associate Chair with the Department of Electrical and Computer Engineering at Northeastern University, Boston, MA. He was a Hearin Hess Distinguished Assistant Professor at Mississippi State University and previously was a Visiting Scientist at the Massachusetts Institute of Technology, Cambridge. He was previously an NSF Presidential Faculty Fellow. He performs research in the areas of power electronics, electric motor drives, and control. A primary focus of his research is in the modeling, design, and control of dc–dc converters.

Prof. Lehman serves as an Associate Editor of the IEEE TRANSACTIONS ON POWER ELECTRONICS and, from 1993 to 1997, served as an Associate Editor for the IEEE TRANSACTIONS ON AUTOMATIC CONTROL. He was the recipient of an Alcoa Science Foundation Fellowship.

Chunxiao Sun (M'03) received the B.S. and M.S. degrees in electrical engineering from Tsinghua University, Beijing, China, in 1991 and 1993, respectively, and the Ph.D. degree in electrical and computer engineering from Northeastern University, Boston, MA, in 2000.

Since 2000, she has been with Danaher Corporation, Wilmington, MA. Her current research interest is in power electronic applications in motor drives, including advanced power inverters, converters, current sensing techniques, and EMI.